






















A Comprehensive X-ray Report on AT2019wey

YUHAN YAO ¹, S. R. KULKARNI ¹, K. C. GENDREAU,² GAURAVA K. JAISAWAL ³, TERUAKI ENOTO ⁴,
BRIAN W. GREFENSTETTE ¹, HERMAN L. MARSHALL ⁵, JAVIER A. GARCÍA ^{1,6}, R. M. LUDLAM ^{1,*},
SEAN N. PIKE ¹, MASON NG ⁵, LIANG ZHANG ⁷, DIEGO ALTAMIRANO ⁷, AMRUTA JAODAND ¹,
S. BRADLEY CENKO ⁸, RONALD A. REMILLARD ⁵, JAMES F. STEINER,⁹ HITOSHI NEGORO ¹⁰, MURRAY BRIGHTMAN,¹
AMY LIEN ^{11,12}, MICHAEL T. WOLFF ¹³, PAUL S. RAY ¹³, KOJI MUKAI,^{14,12} ZORAWAR WADIASINGH ^{8,15},
ZAVEN ARZOUMANIAN,⁸ NOBUYUKI KAWAI,¹⁶ TATEHIRO MIHARA,¹⁷ AND TOD E. STROHMAYER ⁸

¹*Cahill Center for Astronomy and Astrophysics, California Institute of Technology, Pasadena, CA 91125, USA*

²*Mail Code 662.1, Goddard Space Flight Center, Greenbelt, MD 20771, USA*

³*National Space Institute, Technical University of Denmark, Elektrovej 327-328, DK-2800 Lyngby, Denmark*

⁴*Extreme Natural Phenomena RIKEN Hakubi Research Team, Cluster for Pioneering Research, RIKEN,
2-1 Hirosawa, Wako, Saitama 351-0198, Japan*

⁵*MIT Kavli Institute for Astrophysics and Space Research, 70 Vassar Street, Cambridge, MA 02139, USA*

⁶*Dr. Karl Remeis-Observatory and Erlangen Centre for Astroparticle Physics, Sternwartstr. 7, 96049 Bamberg, Germany*

⁷*Department of Physics and Astronomy, University of Southampton, Southampton, SO17 1BJ, UK*

⁸*Astrophysics Science Division, NASA Goddard Space Flight Center, Greenbelt, MD 20771, USA*

⁹*Harvard-Smithsonian Center for Astrophysics, 60 Garden St., Cambridge, MA 02138, USA*

¹⁰*Department of Physics, Nihon University, 1-8, Kanda-Surugadai, Chiyoda-ku, Tokyo 101-8308*

¹¹*Center for Research and Exploration in Space Science and Technology (CRE SST) and NASA Goddard Space Flight Center, Greenbelt,
MD 20771, USA*

¹²*Department of Physics, University of Maryland, Baltimore County, 1000 Hilltop Circle, Baltimore, MD 21250, USA*

¹³*Space Science Division, U.S. Naval Research Laboratory, Washington, DC 20375, USA*

¹⁴*CRESST II and X-ray Astrophysics Laboratory, NASA/GSFC, Greenbelt, MD 20771, USA*

¹⁵*Universities Space Research Association (USRA), Columbia, MD 21046, USA*

¹⁶*Department of Physics, Tokyo Institute of Technology, 2-12-1 Ookayama, Meguro-ku, Tokyo 152-8551*

¹⁷*Cosmic Radiation Laboratory, RIKEN, 2-1 Hirosawa, Wako, Saitama 351-198*

ABSTRACT

Here, we present *MAXI*, *Swift*, *NICER*, *NuSTAR* and *Chandra* observations of the X-ray transient AT2019wey (SRGA J043520.9+552226, SRGE J043523.3+552234). From spectral and timing analyses we classify it as a Galactic low-mass X-ray binary (LMXB) with a black hole (BH) or neutron star (NS) accretor. AT2019wey stayed in the low/hard state (LHS) from 2019 December to 2020 August 21, and the hard-intermediate state (HIMS) from 2020 August 21 to 2020 November. For the first six months of the LHS, AT2019wey had a flux of ~ 1 mCrab, and displayed a power-law X-ray spectrum with photon index $\Gamma = 1.8$. From 2020 June to August, it brightened to ~ 20 mCrab. Spectral features characteristic of relativistic reflection became prominent. On 2020 August 21, the source left the “hard line” on the rms–intensity diagram, and transitioned from LHS to HIMS. The thermal disk component became comparable to the power-law component. A low-frequency quasi-periodic oscillation (QPO) was observed. The QPO central frequency increased as the spectrum softened. No evidence of pulsation was detected. We are not able to decisively determine the nature of the accretor (BH or NS). However, the BH option is favored by the position of this source on the Γ – L_X , L_{radio} – L_X , and L_{opt} – L_X diagrams. We find the BH candidate XTE J1752–223 to be an analog of AT2019wey. Both systems display outbursts with long plateau phases in the hard states. We conclude by noting the potential of *SRG* in finding new members of this emerging class of low luminosity and long-duration LMXB outbursts.

Corresponding author: Yuhan Yao

yyao@astro.caltech.edu

1. INTRODUCTION

Low-mass X-ray binaries (LMXBs) contain a neutron star (NS) or black hole (BH) accretor and a low-mass ($\lesssim 2 M_{\odot}$) companion star. To first order, LMXBs with higher mass transfer rates (\dot{M}) can keep the accretion disks fully ionized, and are observed as persistent sources. Systems with lower \dot{M} exhibit prolific outbursts, which are popularly attributed to the thermal-viscous instability (Tanaka & Shibazaki 1996; Done et al. 2007; Coriat et al. 2012).

Transient BH LMXBs have been observed in several distinct X-ray states, including the steep power-law (SPL) state (also known as the very high state), the high/soft state (HSS; also known as the thermal state), the intermediate state (IMS), the low/hard state (LHS), and the quiescent state (Fender et al. 2004; Remillard & McClintock 2006; McClintock & Remillard 2006; Belloni 2010; Gilfanov 2010; Zhang 2013). This classification scheme relies primarily on the shape of the 1–20 keV energy spectrum, the spectral hardness (defined as the ratio of count rates in the hard and soft energy bands), the fractional rms variability integrated over a range of frequencies, and the presence of quasi-periodic oscillation (QPO) in the power density spectrum (PDS).

The evolution of a BH outburst is traditionally described as a counterclockwise q-shaped track in the hardness–intensity diagram (HID; Homan & Belloni 2005), following the sequence of quiescence \rightarrow LHS \rightarrow IMS \rightarrow HSS \rightarrow IMS \rightarrow LHS \rightarrow quiescence. In the LHS, the X-ray spectrum is dominated by a non-thermal power-law component with a photon index (Γ) of 1.5–2.0. This state is commonly accompanied by strong aperiodic variability and low-frequency QPO (LFQPO; 0.1–30 Hz), with fractional rms of $\sim 30\%$. In the IMS, a thermal disk component with a color temperature of 0.1–1 keV appears and Γ softens to 2.0–2.5. The IMS can be further separated into the hard-intermediate state (HIMS), where the fractional rms is $\sim 10\text{--}20\%$, and the soft-intermediate state (SIMS), where the fractional rms is a few percent (Belloni 2010). In the HSS, the thermal accretion disk becomes the dominant component in the X-ray spectrum. Meanwhile, QPOs are absent or very weak, and the fractional rms drops to $\sim 1\%$. Occasionally, the outburst goes into the SPL state as it approaches the Eddington luminosity L_{Edd} . Here, the spectrum is dominated by a power-law spectral component with a photon index of $\Gamma \sim 2.5$.

Although a good number of BH LMXB outbursts follow the above hysteresis loop of state transition, some remain in the LHS throughout the entire outburst (Belloni et al. 2002a; Brocksopp et al. 2004; Sidoli et al. 2011), and some only transition between the LHS and the HIMS (Ferrigno et al. 2012; Soleri et al. 2013; Capitanio et al. 2009). By analyzing the BH outbursts between 1996 and 2015, Tetarenko et al. (2016) show that $\sim 40\%$ of them only stay in the LHS or HIMS. These “hard-only” outbursts (also termed as failed outbursts) are generally associated with lower peak luminosities.

NS LMXBs can be broadly classified into Z sources and atoll sources, named after the tracks they trace out in the HID and X-ray color-color diagram (Hasinger & van der Klis 1989; van der Klis 2006). Z sources are generally bright ($L_{\text{X}} \gtrsim 0.5L_{\text{Edd}}$). Atoll sources are further divided into bright atoll sources (BA; $L_{\text{X}} \sim 0.3\text{--}0.5L_{\text{Edd}}$) and ordinary atoll sources ($L_{\text{X}} \sim 0.01\text{--}0.3L_{\text{Edd}}$). The X-ray spectra of Z and BA sources remain very soft, while ordinary atolls mostly follow the hysteresis pattern of state transition observed in BH LMXBs (Muñoz-Darias et al. 2014).

BHs can be identified via dynamical measurements of the mass of the compact object. NS LMXBs can be selected by the existence of thermonuclear X-ray bursts from nuclear burning of the accreted material on the NS surface, or coherent pulsations caused by the magnetic field and NS rotation (Lewin et al. 1993; Done et al. 2007; Bhattacharyya 2009).

Kilo-hertz QPOs have only been observed in NS systems (van Doesburgh et al. 2018). Furthermore, in the hard state, NSs have systematically lower values of Compton y -parameter and electron temperature (Banerjee et al. 2020), as well as higher values of Γ (Wijnands et al. 2015). Compared with BH LMXBs, the PDS of NS systems can show broad-band noise at frequencies up to 500 Hz (Sunyaev & Revnivtsev 2000). In the soft state, the spectra of NS LMXBs are harder than those of BH systems due to an additional thermal emission from the boundary layer with a blackbody temperature of ~ 2.4 keV (Done & Gierliński 2003; Gilfanov et al. 2003).

1.1. AT2019wey

AT2019wey was discovered as an optical transient by the ATLAS optical survey in 2019 December (Tonry et al. 2019). It rose to prominence in 2020 March with the discovery of X-ray emission by the eROSITA (Predehl et al. 2021) and the Mikhail Pavlinsky ART-XC (Pavlinsky et al. 2021) telescopes on board the *Spektrum-Roentgen-Gamma* (SRG) satellite (Sunyaev

* NASA Einstein Fellow

et al. 2021). Upon detection, the X-ray flux was 0.36 mCrab in the 0.3–8 keV band and 0.6 mCrab in the 4–12 keV band (Mereminskiy et al. 2020). We note that there is no point source detected at the position of AT2019wey in the 2nd *ROSAT* All-Sky Survey Point Source Catalog (2RXS; Boller et al. 2016), providing a historical upper limit of $\sim 10 \mu\text{Crab}$ in 0.1–2.4 keV.

Initially AT2019wey was thought to be a supernova (Mereminskiy et al. 2020) and subsequently proposed to be a BL Lac object (Lyapin et al. 2020). Yao et al. (2020b) reported the detection of hydrogen lines at redshift $z = 0$, and proposed AT2019wey to be a Galactic accreting binary.

Here, we report comprehensive X-ray observations from the beginning of 2019 January to the end of 2020 November. We find that AT2019wey is consistent with the spectral and timing behavior expected from a LMXB harbouring a BH or NS accretor. Elsewhere we report the multi-wavelength observations of this source (Yao et al. 2020c, hereafter Paper II).

This paper is organized as follows. In Section 2 we describe the X-ray observations and data reduction. We present the analysis of light curves in Section 3, including the evolution of hardness (Section 3.1) and the timing properties (Section 3.2). The spectral analysis including multi-mission joint analysis can be found in Section 4. In Section 5 we present the inferences from the X-ray analysis. We are not able to decisively identify the nature of the accretor (BH or NS). However, we find the best analog to AT2019wey is a candidate BH LMXB system. We conclude in Section 6.¹

2. OBSERVATIONS AND DATA REDUCTION

The data shown here were obtained using the Neutron Star Interior Composition Explorer (*NICER*; Gendreau et al. 2016), the Nuclear Spectroscopic Telescope ARray (*NuSTAR*; Harrison et al. 2013), the *Chandra* X-ray Observatory (Wilkes & Tucker 2019), the *Neil Gehrels Swift Observatory* (Gehrels et al. 2004), and the Monitor of All-sky X-ray Image (*MAXI*) mission (Matsuoka et al. 2009). As of the time of submission of the paper (2020 November), the source was still active.

2.1. *NICER*

AT2019wey was observed by the X-ray Timing Instrument (XTI) on board *NICER* over the period from 2020 August 4 to 2020 September 30 (PI: K. Gendreau). The observation log is shown in Table 7. *NICER* is a soft X-ray telescope on board the International Space Station (ISS). *NICER* is comprised of 56 co-aligned con-

centrator X-ray optics, each paired with a single-pixel silicon drift detector. Presently, 52 detectors are active with a net peak effective area of $\sim 1900 \text{ cm}^2$ at 1.5 keV, and 50 of these were selected (excluding modules 14 and 34) to make the light curves reported in this paper. The *NICER* observations were processed using *HEASOFT* version 6.27 and the *NICER* Data Analysis Software (*nicerdas*) version 7.0 (2020-04-23_V007a).

To generate a background-subtracted light curve, we first defined good time intervals (GTIs) with as much data as possible. Then we computed the background using the *nibackgen3C50* tool (Remillard et al. 2021). For each GTI, we explicitly subtracted the background-predicted spectrum from the raw extraction to get the source net spectrum. We also removed GTIs with $|hbg|^2 > 0.07$, to exclude GTIs with less accurate background subtraction. Finally, we computed count rate in five energy bands: 0.4–1.0 keV, 1–2 keV, 2–4 keV, 4–12 keV, and 0.4–12 keV.

To generate spectral files, we used *nimaketime* to select GTIs that occurred when the particle background was low ($KP < 5$ and $COR_SAX > 4$). We removed times of extreme optical light loading and low Sun angle by selecting $FPM_UNDERONLY_COUNT < 200$ and $SUN_ANGLE > 60$. Using *niextract-events*, the GTIs were applied to the data selecting $EVENT_FLAGS = bxxx1x000$ and PI energy channels between 25 and 1200, inclusive. For more information on the *NICER* screening flags, see Bogdanov et al. (2019). The resulting event files were loaded into *xselect* to extract a combined spectrum after filtering. Systematic errors of 1% in the 2–10 keV band and 5% in the 0.8–2 keV band were added via *grppha*. A background spectrum was generated using the *nibackgen3C50* tool for each cleaned event file and ufa event file pair. These were then combined into a single background spectrum that was weighted by the duration of each observation. Each spectrum was grouped into channels by considering a minimum of 32 counts per channel bin.

2.2. *NuSTAR*

We obtained three epochs of Target of Opportunity (ToO) observations using the hard X-ray telescope *NuSTAR* (PI: Y. Yao, Table 8). In this paper, we report the analysis for the first two sequences (sequence IDs 90601315002 and 90601315004, hereafter 002 and 004, respectively). The third sequence was carried out jointly with the Hard X-ray Modulation Telescope (HXMT;

¹ UT time is used throughout the paper.

² *hbg* is the count rate in the 13–15 keV band, which is beyond the effective area of the concentrator optics, as defined in Remillard et al. (2021).

Zhang et al. 2020b), and will be reported in Tao et al. in prep.

The focal plane of *NuSTAR* consists of two photon counting detector modules (FPMA and FPMB). The data were processed using the *NuSTAR* Data Analysis Software (*nustardas*) v2.0.0 along with the 2020423 *NuSTAR* CALDB using the default data processing parameters. Cleaned event files were produced with *nupipeline*. The event files were then barycentered and corrected for clock offset using *barycorr*³.

To generate *NuSTAR* light curves, we filtered the events using source regions with radii of 60'' and 90'' for 002 and 004, respectively. We chose to use a larger source region for observation 004 due to its higher count rate. We only retained events with a photon energy between 3 and 78 keV. For each observation, we were thus left with two lists of filtered and barycenter-corrected events — one for FPMA and one for FPMB. Using *Stingray* (Huppenkothen et al. 2019), we produced light curves for each of these event lists. We binned the light curves with a time resolution of ≈ 2 ms. *Stingray* automatically applied the GTIs recorded by the instrument.

To generate the spectra for FPMA and FPMB, source photons were extracted from a circular region with a radius of 60'' centered on the apparent position of the source in both FPMA and FPMB. For 002 the background was extracted from a 100'' region located on the same detector; For 004 the source was bright enough that a smaller portion of the field-of-view could be used to estimate the background, so the background was extracted from a 60'' region.

2.3. *Chandra*

We requested and were granted 25 ks of *Chandra* director’s discretionary time (PI: S. R. Kulkarni; OBSID = 24651) to obtain a high-energy transmission grating spectrometer (HETGS; Markert et al. 1994; Canizares et al. 2005) spectrum using the Advanced CCD Imaging Spectrometer (ACIS; Garmire et al. 2003). The HETGS is composed of two sets of gratings (see, e.g., Chapter 2 of Wilkes & Tucker 2019): the medium-energy gratings (MEGs) cover the 0.4–7 keV energy band, and the high-energy gratings (HEGs) cover the 0.8–10.0 keV band. The observation was carried out in the timed event (TE) mode around the maximum soft X-ray luminosity of AT2019wey. During the exposure (from 2020-09-20T17:43 to 2020-09-21T01:12), the source count rate varied between 23.1 count s⁻¹ to 24.5 count s⁻¹.

³ We used the clockfile version v108. See Bachetti et al. (2021) for a description of the clockfile generation.

To generate spectral files for the source and the background, we extracted the plus and minus first-order ($m = \pm 1$) MEG and HEG data from the -1 and the $+1$ arms of the MEG and HEG gratings. We used the CIAO tool *tgextract*. CIAO version 4.12.1 and the associated CALDB version 4.9.3 were used in the data reduction. Spectral redistribution matrix files and effective area files were generated with *mkgrmf* and *mkgarf*.

2.4. *MAXI*

MAXI was installed on the Japanese Experiment Module Exposed Facility on the ISS in 2009 July. Since 2009 August, the *MAXI* Gas Slit Cameras (GSCs; Mihara et al. 2011; Sugizaki et al. 2011) have been observing the source region of AT2019wey in the 2–20 keV band every 92 min synchronized with the ISS orbital period. Owing to the ISS orbit precession of about 72 days, the source region, due to the interference of some structure of the detectors, has been regularly unobservable for about 12 days. Furthermore, in recent years, the source has only been observed with the degraded cameras for ~ 28 days in each precession period. We did not use these data. As a result, there are two data gaps every 72 days.

The 1-day average *MAXI* light curves were generated by the point-spread-function fit method (Morii et al. 2016) to obtain the most reliable curves in the 2–4 keV and 4–10 keV bands. Furthermore, we excluded data with 1σ uncertainties 2.5 times larger than the average uncertainties in the 2–4 and 4–10 keV bands, respectively. We rebinned the data into 4-day bins to improve the statistics.

2.5. *Swift*

2.5.1. *XRT*

AT2019wey was observed by the X-Ray Telescope (XRT; Burrows et al. 2005) on board *Swift* in 2020 April (4 epochs), August (5 epochs), and September (4 epochs). We generated the X-ray light curve for AT2019wey using an automated online tool⁴ (Evans et al. 2009). The first 9 epochs were obtained in Photon Counting (PC) mode, and thus suffer from “pile-up” at the high observed count rates. Standard corrections (Evans et al. 2007) were applied to the observations taken in 2020 April. The observations from 2020 August were sufficiently piled up that no reliable count rates could be obtained. Beginning in 2020 September, XRT observations were obtained in Window Timing (WT) mode, where larger count rates can still be

⁴ https://www.swift.ac.uk/user_objects



Figure 1. *Upper:* *NICER* and *MAXI* light curves of AT2019wey in the 2–10 keV band. The dark blue arrow marks the epoch of *SRG* discovery. The black arrow marks the epoch of *Chandra* observation. *Middle:* *MAXI* light curves in the 2–4 keV and 4–10 keV bands. The magenta arrows mark epochs of *Swift/XRT* observations (Table 9). *Bottom:* *Swift/BAT* light curve of AT2019wey in the 15–50 keV band. The blue arrows mark epochs of *NuSTAR* observations (Table 8). The dashed vertical line in all three panels marks the optical first detection epoch.

reliably measured. The observation log and the count rate measurements are shown in Table 9.

To generate XRT spectra for the 4 epochs obtained in 2020 April, we processed the data using `xrtproducts`. We extracted source and background photons from circular regions with radii of $50''$ and $100''$, respectively.

2.5.2. BAT

Since 2004 November, the source region of AT2019wey has been observed by the Burst Alert Telescope (BAT; Krimm et al. 2013) on board *Swift*. The 15–50 keV BAT light curve is provided by the “scaled map” data prod-

uct⁵. To generate a light curve with better statistics, we rebinned the light curve into 4-day bins, and excluded data with 1σ uncertainties 3 times larger than the median uncertainties.

3. ANALYSIS OF LIGHT CURVES

The *MAXI*, *NICER*, and *Swift/BAT* light curves of AT2019wey are shown in Figure 1. The dashed vertical lines in the three panels mark the epoch of first

⁵ Available at <https://swift.gsfc.nasa.gov/results/transients/weak/AT2019wey/>.

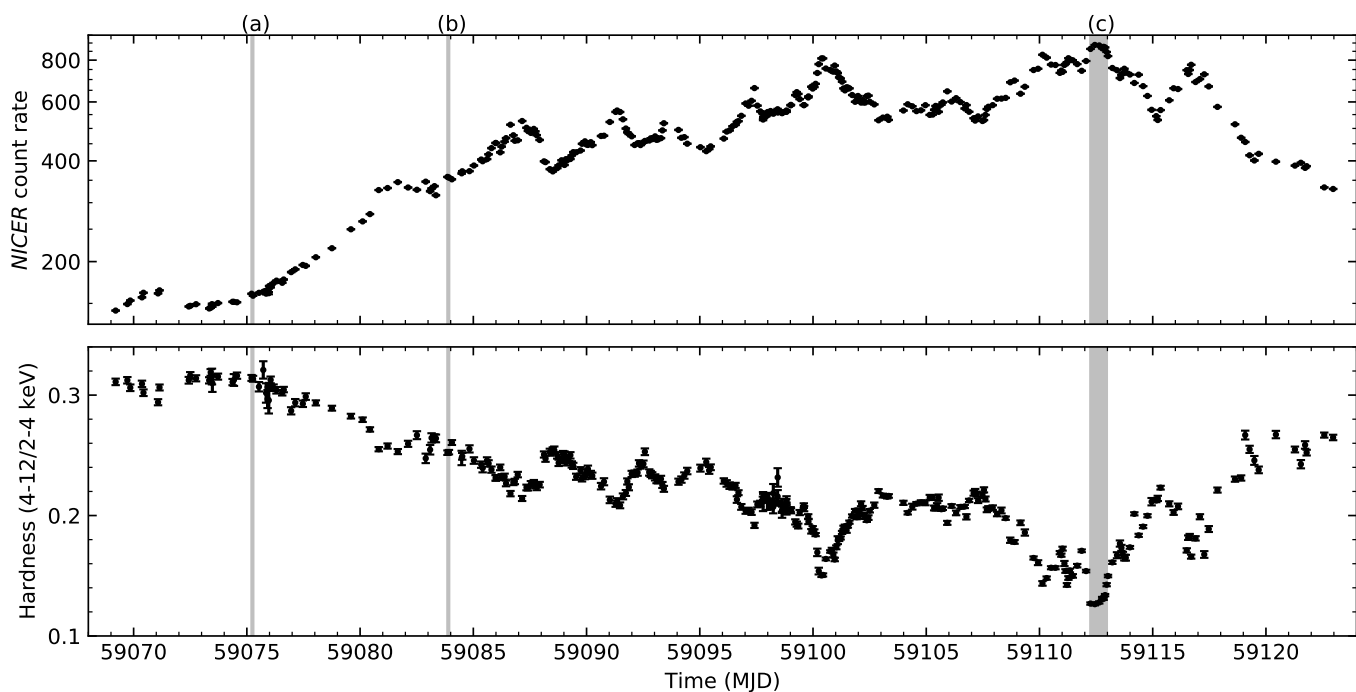


Figure 2. *Upper:* *NICER* (0.4–12 keV) light curve of AT2019wey. *Bottom:* *NICER* hardness (ratio of the 4–12 keV and 2–4 keV count rates) of AT2019wey. The three vertical grey regions mark epochs where detailed timing analysis are performed (see Section 3.2.1 and Table 1.)

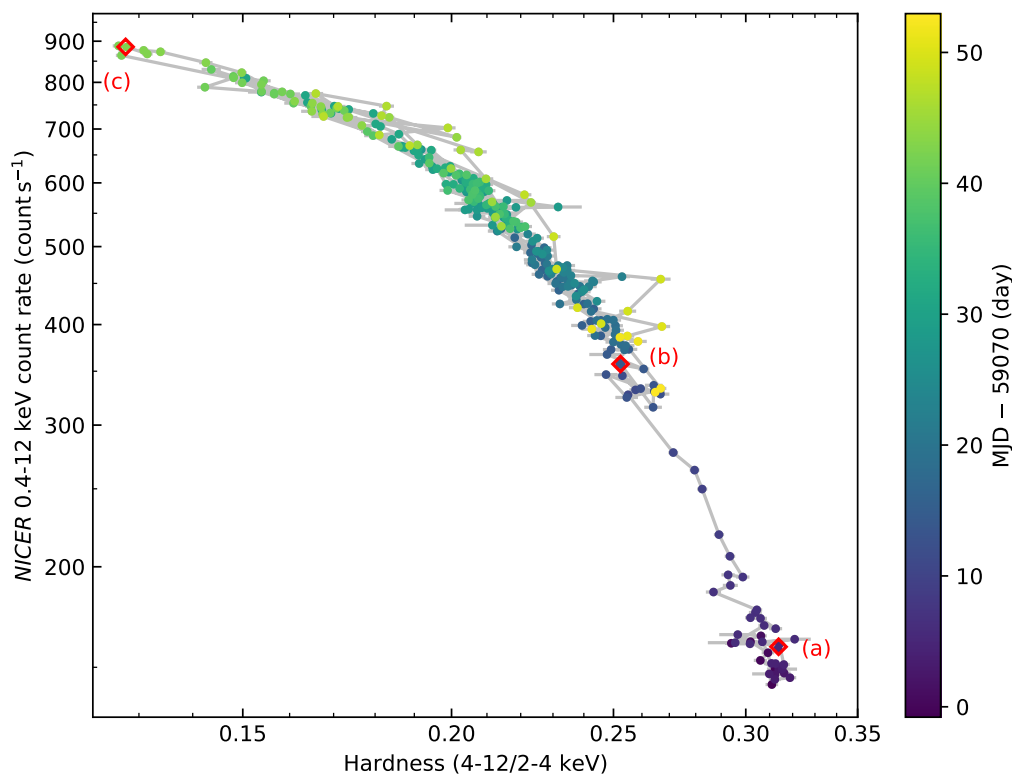


Figure 3. The *NICER* HID, defined as the 0.4–12 keV count rate versus the hardness (ratio of the 4–12 keV and 2–4 keV count rates). The data points are color coded by time. The three red diamonds mark epochs where detailed timing analysis are performed (see Section 3.2.1 and Table 1.)

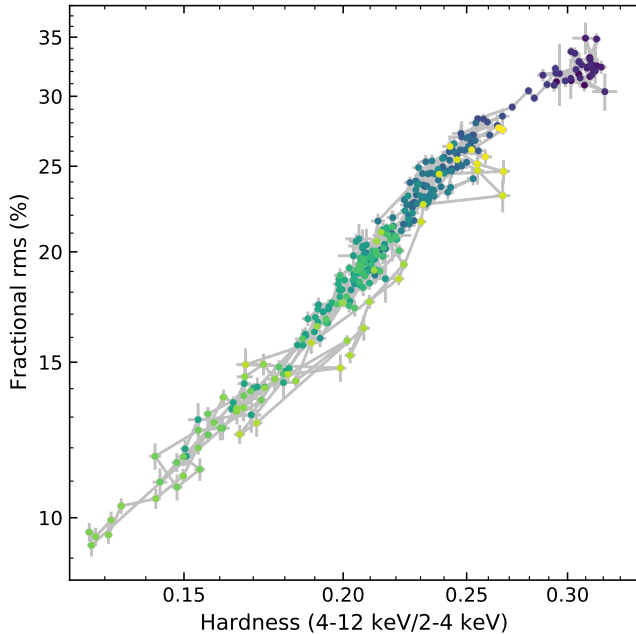


Figure 4. The *NICER* HRD, defined as the hardness versus the fractional rms integrated in the 0.1–64 Hz frequency range. The data is color-coded by time following the scale shown in Figure 3.

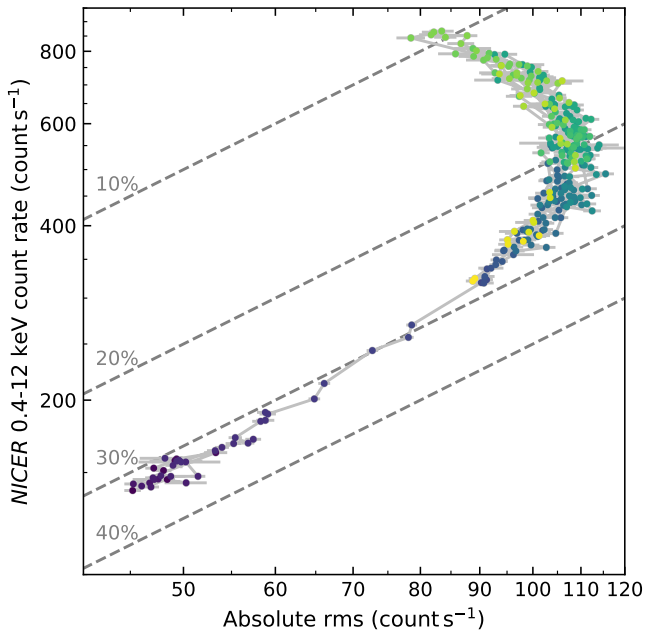


Figure 5. The *NICER* RID, defined as the absolute rms versus the 0.4–12 keV count rate. The gray dotted lines represent the 10, 20, 30 and 40 percent fractional rms levels. The data is color-coded by time following the scale shown in Figure 3.

optical detection on 2019 December 2 (Paper II). From 2019 January 1 to December 2, the *MAXI*/GSC and *Swift*/BAT data show no significant count excess. We refer to Hori et al. (2018) for *MAXI*/GSC detection upper limits during the period from 2009 August 13 to 2016 July 31. From the 2019 December 2 to the *SRG* discovery epoch (2020 March 18), *MAXI*/GSC detected a significant 2–10 keV flux excess of 1.7 ± 0.4 mCrab (see Negoro et al. 2020), and BAT detected a significant 15–50 keV flux excess of 3.7 ± 0.7 mCrab.

As can be seen from the *MAXI* and BAT light curves, the source started to significantly brighten from the beginning of 2020 June to the middle of 2020 August. Since then, the source has stayed at a relatively high level of flux. From 2020 September 2 to 2020 November 30, the median *MAXI* 2–10 keV flux is 17.7 mCrab and the median BAT 15–50 keV flux is 28.1 mCrab. The *NICER* light curve is presented in the upper panel of Figure 2. It clearly shows that after the X-ray brightening, AT2019wey underwent a few week-long mini-outbursts in the 0.4–12 keV band.

3.1. Hardness Evolution

We define the X-ray hardness (or X-ray color) using the ratio of count rates in the *NICER* 4–12 keV and 2–4 keV bands. The evolution of hardness is shown in the bottom panel of Figure 2. Figure 3 presents the *NICER* HID of AT2019wey. At the beginning, the source was faint and hard. As it got brighter, the X-ray color became softer. The count rate (hardness) reached the maximum (minimum) value at 59112 MJD, after which the count rate decreased and the X-ray color hardened. The evolution of AT2019wey roughly follows a single line on the HID, i.e., each hardness value corresponds to a single value of count rate. This is very different from the hysteresis pattern generally observed in LMXBs.

3.2. Timing Properties

The typical event timestamps for *NICER*/XTI and *NuSTAR* are accurate to ~ 100 ns (Prigozhin et al. 2016) and $\sim 100 \mu\text{s}$ (Bachetti et al. 2021), respectively. The high timing precision makes the two instruments ideal to study fast X-ray variability. We searched for coherent pulsation signals in the *NICER* and *NuSTAR* data and found no viable pulse search candidates to 3σ level despite pulsation searches extending to 100 ns (see Appendices B.1 and B.2 for details). Here, we present aperiodic analysis of *NICER* (Section 3.2.1) and *NuSTAR* (Section 3.2.2) observations.

3.2.1. *NICER* Aperiodic Analysis

We produced an average PDS in the 0.5–12 keV energy band for each GTI. We used 16-s long intervals and

≈ 0.12 ms time resolution. The average PDS was rms-normalized (Belloni & Hasinger 1990) and the contribution due to the photon counting noise was subtracted. We calculated the integrated fractional rms in the 0.1–64 Hz frequency range. We also calculated the absolute rms by multiplying the fractional rms by the net count rate (Muñoz-Darias et al. 2011).

In Figure 4 we show the hardness–fractional rms diagram (HRD), which is usually used to study the outburst evolution of transient BH LMXBs (Belloni et al. 2005). The integrated fractional rms decreased from $\sim 30\%$ to $\sim 10\%$ as the X-ray color softened, and increased back to $\sim 25\%$ as the color hardened again.

In Figure 5 we show the absolute rms–intensity diagram (RID). At the beginning of the X-ray brightening, we found that the absolute rms increased with the count rate. This linear trend has been observed in many BH binaries, and is commonly known as the “hard line” (HL; Muñoz-Darias et al. 2011). Starting from ~ 59082 MJD, the source left the HL and moved upwards. During the light curve bumps observed between ~ 59085 MJD and ~ 59123 MJD, the source moved to the left as the count rate increased, and then went back as the count rate decreased.

During the period we analyzed, the PDS can be well fitted with two or three Lorentzian functions following the prescription laid out by Belloni et al. (2002b). In Figure 6 we show three representative PDS averaged from different phases of the outburst (marked as grey regions in Figure 2 and red diamonds in Figure 3).

Table 1. *NICER* power spectral components

TIME (MJD)		ν_{\max} (Hz)	Q	rms (%)
59075.20–59075.29	L_1	0.33 ± 0.02	0.25 ± 0.08	27.57 ± 1.12
	L_2	1.76 ± 0.14	0.44 ± 0.12	16.33 ± 1.62
59083.85–59083.94	L_1	0.59 ± 0.02	0.26 ± 0.04	24.62 ± 0.34
	L_2	2.06 ± 0.03	6 (fixed)	3.95 ± 0.41
	L_3	3.53 ± 0.16	0.81 ± 0.14	10.17 ± 0.69
59112.24–59112.98	L_1	2.21 ± 0.03	0.34 ± 0.02	9.72 ± 0.07
	L_2	6.58 ± 0.21	4.99 ± 1.97	1.64 ± 0.26

The main properties of the PDS are listed in Table 1. At the beginning of the outburst, the PDS were dominated by strong band-limited noise without showing any significant QPOs. The average PDS can be fitted with two broad Lorentzians (Figure 6 (a)). Starting from ~ 59083 MJD, a weak QPO was sometimes observed in

the PDS. The characteristic frequency of the QPO increased from ~ 2 Hz to ~ 6.5 Hz as the spectra softened. Figure 6 (b)–(c) show the PDS of the QPO with the lowest and highest frequency, respectively. Based on the properties of the QPO and noise, this QPO is similar to the type-C QPO (e.g. Casella et al. 2005; Motta et al. 2011; Ingram & Motta 2019; Zhang et al. 2020a) commonly observed in BH and NS binaries (see, e.g., Klein-Wolt & van der Klis 2008).

3.2.2. *NuSTAR* Aperiodic Analysis

Rather than summing the FPMA and FPMB light curves and producing PDS for each observation, we chose to analyze the Cross Power Density Spectrum (CPDS; Bachetti et al. 2015). The CPDS taken between FPMA and FPMB is given by

$$C(\nu) = \mathcal{F}_A^*(\nu)\mathcal{F}_B(\nu) \quad (1)$$

where $\mathcal{F}_A^*(\nu)$ is the complex conjugate of the Fourier transform of the light curve observed by FPMA and $\mathcal{F}_B(\nu)$ is the Fourier transform corresponding to FPMB. The real part of the CPDS, called the cospectrum, represents only the power of the signals which are in phase between the two light curves, and its imaginary part gives the power of those signals which are in quadrature. The CPDS can therefore be used to calculate time lags and correlations between two light curves.

In order to produce a cospectrum for each observation, we split the light curves observed by each FPM into intervals of 256 s each, resulting in 150 intervals for observation 002 and 173 intervals for observation 004. For each of these intervals, we produced a cospectrum, and then averaged these cospectra together. The frequencies sampled are limited to the range $4 \text{ mHz} < \nu < 256 \text{ Hz}$. The low end of this range is determined by the interval length, and the high end is determined by the sampling rate of the light curves. The resulting averaged, rms-normalized cospectra for observations 002 and 004 are shown in black in Figure 7, where they have been rebinned for clarity. All errors quoted are $1\text{-}\sigma$.

Similar to our analysis in Section 3.2.1, we fit the cospectra with a model consisting of a sum of Lorentzian functions following Belloni et al. (2002b). We used an automated modeling algorithm that fits a cospectrum to composite Lorentzian models with progressively more components, halting when the addition of a component no longer results in the reduction of the χ^2 fit statistic. We chose the model with the minimum number of components which still resulted in a significant improvement to the fit ($|\Delta\chi^2| > 10$), and discarded more complex models with only marginally better fit statistics. For observation 002, this resulted in a single-component

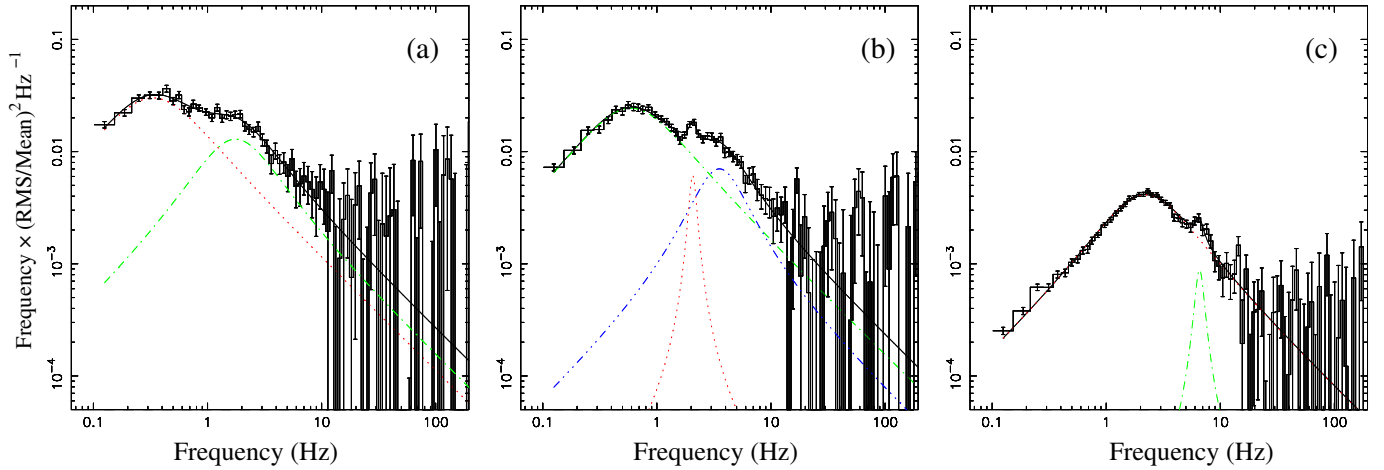


Figure 6. Representative *NICER* power spectra. The power spectra were calculated in the 0.5–12 keV energy band. The main properties of the power spectra are listed in Table 1. The PDS is fitted with a combination of two or three Lorentzian functions, as shown by the colored components in each panel.

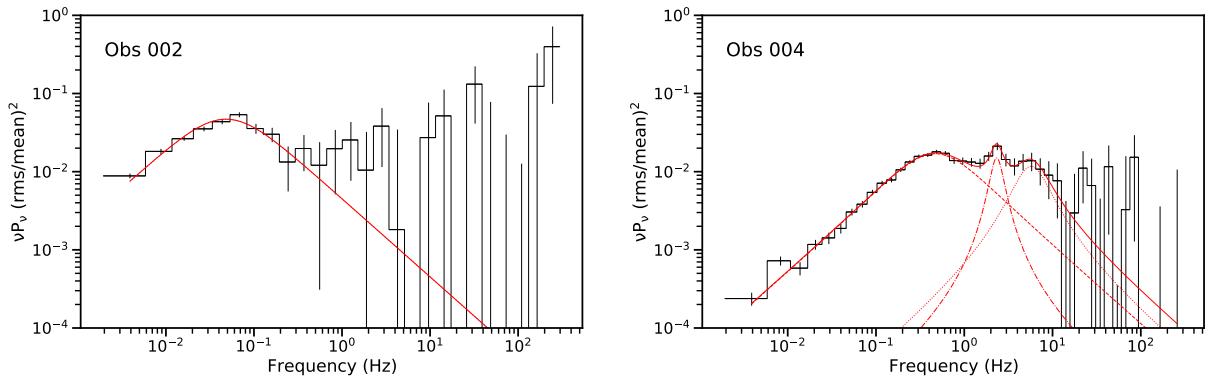


Figure 7. The averaged rms-normalized cospectra for each *NuSTAR* observation are shown in black in units of Power \times Frequency. Their best-fit models are plotted in solid red and the individual Lorentzian components, L_b , L_{LF} , and L_h , are shown in dashed, dashed-dotted, and dotted red, respectively. Cospectra have been rebinned for legibility.

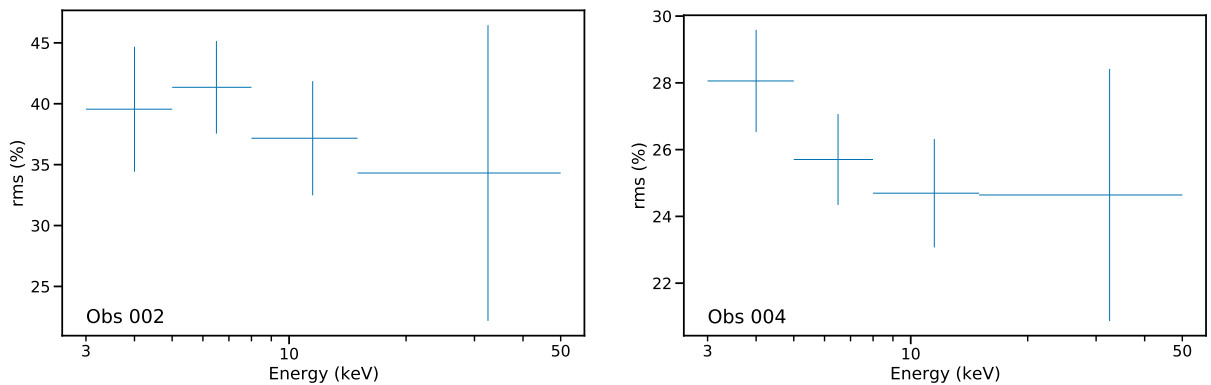


Figure 8. The observed variability as measured by the fractional rms is shown as a function of photon energy for *NuSTAR* observations. While observation 002 is consistent with a flat rms-energy relation, observation 004 shows evidence of decreasing variability with increasing energy.

model containing only one broad Lorentzian with unconstrained ν_0 and Q . For observation 004, we obtained a model with two broad components centered at considerably higher frequencies than that of the component obtained for observation 002. Following the notation of Klein-Wolt & van der Klis (2008), we dub the lowest frequency broad components L_b , and the higher frequency broad component observed in observation 004 L_h .

Table 2. *NuSTAR* power spectral components.

OBSID	Component	ν_{\max} (Hz)	Q	rms (%)
90601315002	L_b	0.05^\dagger	$3 \times 10^{-4}\dagger$	54 ± 5
	L_b	0.5 ± 0.1	0.15 ± 0.03	28 ± 1
90601315004	L_h	5.7 ± 1.4	0.9 ± 0.6	14 ± 3
	L_{LF}	2.3 ± 0.1	2.6 ± 1.0	9.5 ± 1.9

[†]The characteristic frequency and quality factor are not constrained for observation 002, therefore errors are not shown for these quantities.

Following the detection of the two broad components in observation 004 using our fitting algorithm, visual inspection suggested the presence of an additional component at ~ 2 Hz. We therefore added a third QPO-like component to the model and saw a small but significant improvement to the fit of $\Delta\chi^2 = -30$. We label this narrower QPO-like component L_{LF} . Defining the QPO significance as the ratio of the integrated power of the component to its error, A/σ_A , the significance of L_{LF} was calculated to be 2.5σ . Note that this component lines up with the QPO seen in the *NICER* PDS (Figure 6 (b)), and it is therefore still significant. All of the components observed in each observation as well as their fitted parameters are listed in Table 2. The components and the resulting composite models are shown in red in Figure 7.

Finally, in order to better understand the physical origins of the source variability, we computed the variability as a function of photon energy for each observation. We produced cospectra in four energy ranges, and determined the fractional rms by integrating the cospectra. Due to the limited frequency range for which significant power was detected, we did not integrate over the entire available frequency range. Rather, for observation 002, we integrated the power between 4 mHz and 1 Hz, while for observation 004, we integrated the power between 4 mHz and 10 Hz. The resulting rms-energy relations are shown in Figure 8. Observation 002 is consistent

with a flat rms-energy relation, whereas observation 004 may exhibit decreasing variability with increasing photon energy.

4. SPECTRAL ANALYSIS

In this section, we examine the spectral evolution of AT2019wey. For this analysis we use `xspec` version 12.11.0 (Arnaud 1996). Uncertainties of model parameters are represented by the 90% confidence intervals, which are estimated by the `error` command in `xspec`.

Below we present joint analysis (i.e., analysis of contemporaneous datasets obtained from several missions) and also specific data sets.

In Section 4.1–4.3, we perform joint spectral analyses of three sets of observations obtained in 2020 April, August, and September. Section 4.1 presents the April 2020 epoch, where the *NuSTAR* 002 spectra for FPMA and FPMB were fitted with data from four *Swift*/XRT observations obtained in April 2020 (Table 9). Section 4.2 presents the August 2020 epoch, where the *NuSTAR* 004 spectra for FPMA and FPMB were fitted with two *NICER* observations bracketing the *NuSTAR* observation (Table 7, OBSID 3201710112 and 3201710113). Section 4.3 presents the September 2020 epoch, where the *Chandra* spectra were fitted with two *NICER* observations bracketing the *Chandra* observation (Table 7, OBSID 3201710147 and 3201710148). In Section 4.4, we analyze the *NICER* spectra for each OBSID between 3201710105 and 3201710157.

Table 3. Best-fit model parameters of the 2020 April joint observations.

Parameter	90% Interval
constant	
$\mathcal{C}_{\text{FPMA}}$	1 (frozen)
$\mathcal{C}_{\text{FPMB}}$	1.037 ± 0.014
\mathcal{C}_{XRT}	$0.796^{+0.039}_{-0.038}$
tbabs	
N_{H} (10^{22} cm $^{-2}$)	$0.609^{+0.049}_{-0.045}$
powerlaw	
Γ	1.765 ± 0.013
norm^\dagger	$9.06^{+0.27}_{-0.26}$
C-stat / d.o.f.	1292.70/1541

[†]Normalization at 1 keV in units of 10^{-3} ph keV $^{-1}$ cm $^{-2}$.

4.1. Joint Analysis, 2020 April

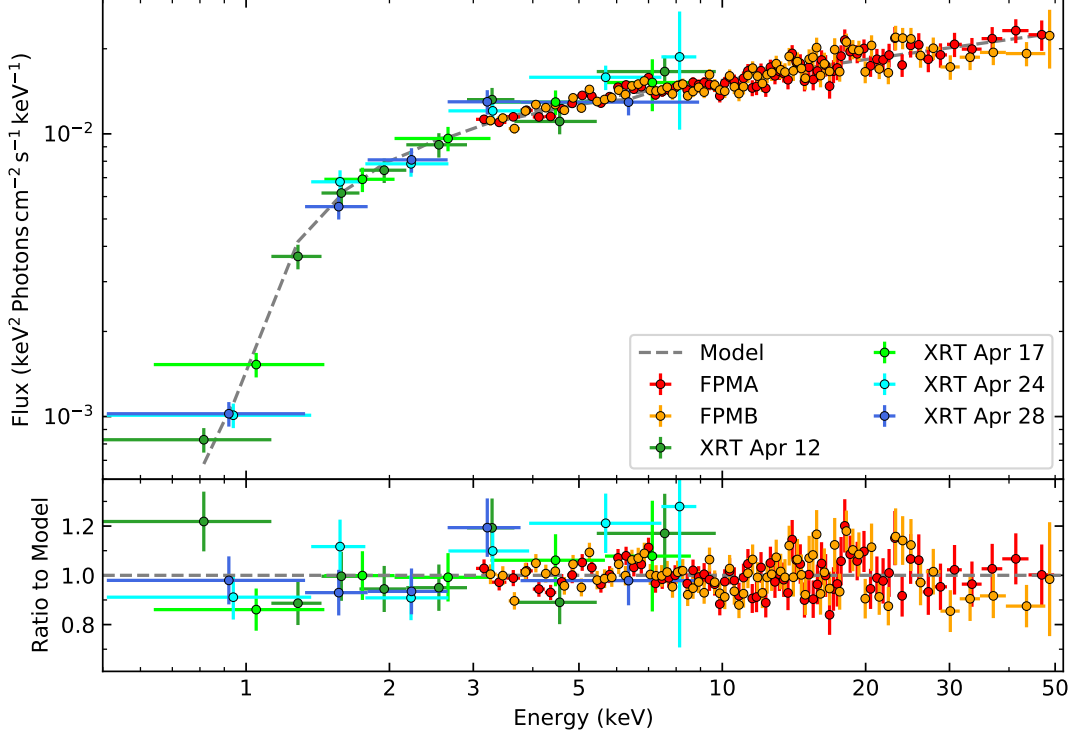


Figure 9. *Upper:* Unfolded spectrum of the data from the two *NuSTAR* detector modules and the four *Swift*/*XRT* observations. The best-fit model for *NuSTAR*-FPMA is shown in the dashed grey line. To account for the cross-normalization terms (see Table 3), the FPMB and XRT data are divided by 1.037 and 0.796, respectively. *Bottom:* The ratio of data to the best-fit model is shown for all three data sets. The data have been rebinned for visual clarity.

The upper panel of Figure 9 shows the *NuSTAR* 002 and *Swift*/*XRT* spectra in April 2020, which appears relatively featureless. We therefore modeled the data with an absorbed power-law (`tbabs*powerlaw`, in `xspec`, Wilms et al. 2000). We also included a leading cross-calibration term (`constant`; Madsen et al. 2017) between the two *NuSTAR* telescopes (with C_{FPMA} defined to be 1) and a single term used for all four *Swift*/*XRT* observations. The four XRT spectra were grouped with `grppha` to have at least one count per bin. The *NuSTAR* FPMA and FPMB spectra were grouped with `ftgrouppha` using the optimal binning scheme developed by Kaastra & Bleeker (2016). All data were fitted using *C*-statistics via `cstat` (Cash 1979). For *NuSTAR* we fitted the data over the 3–50 keV range as the source spectrum becomes comparable to the background at higher energies, while for *Swift* we fitted from 0.5 to 10 keV.

The best-fit model is shown in Figure 9. The model parameters are given in Table 3. We note that the C_{XRT} is lower than we would typically expect. A probable explanation is that the pile-up resulted in an observed flux lower than expected, as the source count rate is relatively high for the XRT PC mode (see Table 9).

The unabsorbed flux in the 0.3–100 keV band for FPMA is $1.4 \times 10^{-10} \text{ erg cm}^{-2} \text{ s}^{-1}$. Paper II constrains the distance of AT2019wey to be $1 \lesssim D \lesssim 10 \text{ kpc}$. At distances of [1, 3, 5, 10] kpc, this corresponds to a luminosity of $[0.16, 1.5, 4.1, 16.3] \times 10^{35} \text{ erg s}^{-1}$. The Eddington luminosity is $L_{\text{Edd}} = 1.46 \times 10^{38} (M/M_{\odot}) \text{ erg s}^{-1}$ (assuming solar hydrogen mass fraction $X = 0.71$). Therefore, the X-ray luminosity in 2020 April is $10^{-5} \lesssim L_X/L_{\text{Edd}} \lesssim 10^{-3}$ for a $\approx 10 M_{\odot}$ compact object.

4.2. Joint Analysis, 2020 August 16

The upper panel of Figure 10 shows the *NuSTAR* 004 and simultaneous *NICER* spectra, and the bottom panel presents the ratio of data to an absorbed power-law model (`tbabs*powerlaw`) fitted only to the 3–4 keV and 10–12 keV energy bands ($\Gamma \sim 1.8$). As reported by Yao et al. (2020a), we clearly detected the broadened Fe $K\alpha$ line and Compton hump, characteristic of the relativistic reflection spectrum commonly seen in accreting X-ray binaries (García et al. 2011).

We modeled the spectrum by a combination of disk blackbody and relativistic reflection from an accretion disk (`tbfeo*edge*(simplcutx*diskbb+relxillCp)`, in `xspec`). In this model, the continuum is assumed to

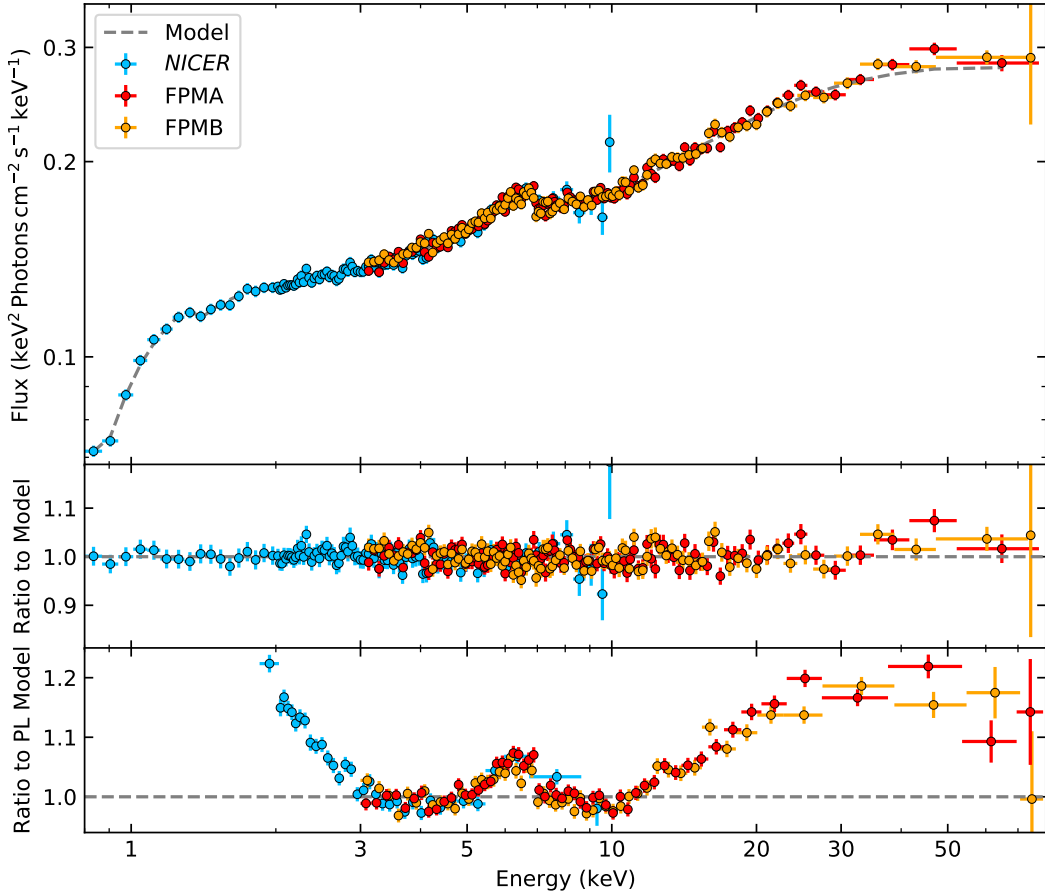


Figure 10. *Upper:* Unfolded spectrum of the joint *NuSTAR* and *NICER* observations. The best-fit model for *NuSTAR*-FPMA is shown in the dashed grey line. To account for the cross-normalization terms (see Table 4), the FPMB and *NICER* data are divided by 1.051 and 1.035, respectively. *Middle:* The ratio of data to the best-fit model. *Bottom:* The ratio of data to a simple power-law model. The model is fitted only to the 3–4 keV and 10–12 keV energy ranges. The data have been rebinned for visual clarity.

be produced by Comptonization of the disk photons (`simplcut*diskbb`, Steiner et al. 2017; Mitsuda et al. 1984), and the reflection is fitted with a `relxill` model (García et al. 2014; Dauser et al. 2014) that incorporates such continuum (`relxillCp`). A photoelectric absorption (`edge`) was added to account for instrumental uncertainties within the spectrum where *NICER*’s calibration is still ongoing (see, e.g., Ludlam et al. 2020)

All data were fitted using *C*-statistics. For *NuSTAR* we fitted the data over the 3–79 keV range, while for *NICER* we fitted from 0.8 to 10 keV. The *NuSTAR* data were grouped to have signal-to-noise ratio of 6 and oversampling factor of 3. Details of the model fitting are presented in Appendix B.3. The best-fit model is shown in Figure 10. The model parameters are given in Table 4.

The best-fit reflection spectrum is analogous to those observed in other black hole binaries, such as GX 339–4 (Wang-Ji et al. 2018) or XTE J1550–564 (Connors et al.

2020). The unabsorbed flux in the 0.3–100 keV band for FPMA is $1.8 \times 10^{-9} \text{ erg cm}^{-2} \text{ s}^{-1}$. At distances of [1, 3, 5, 10] kpc, this corresponds to a luminosity of [0.21, 1.9, 5.3, 21.1] $\times 10^{36} \text{ erg s}^{-1}$. Therefore, the X-ray luminosity on 2020 August 16 is $1.4 \times 10^{-4} \lesssim L_X/L_{\text{Edd}} \lesssim 1.4 \times 10^{-2}$ for a $10 M_{\odot}$ compact object.

4.3. Joint Analysis, 2020 September 20

The upper panel of Figure 11 shows the simultaneous *Chandra* and *NICER* observations. No strong narrow emission or absorption lines were detected in the HETGS spectrum. To model the continuum, we adopted the `constant*tbabs*(simpl*diskbb+gaussian)` model, where `simpl` is a Comptonization model that generates the power-law component via Compton scattering of a fraction (f_{sc}) of input seed photons from the disk (Steiner et al. 2009). The flag R_{up} was set to 1 to

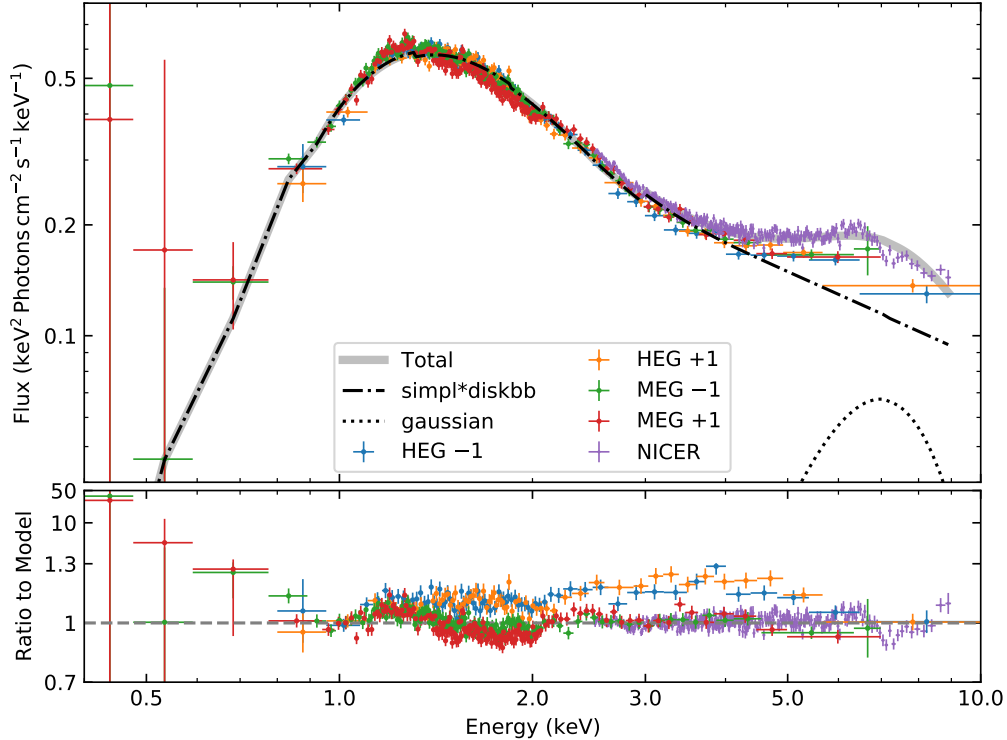


Figure 11. *Upper:* Unfolded spectrum of the joint *Chandra* and *NICER* observations. We show the best-fit model for *NICER* above 4.0 keV, and the best-fit model for MEG –1 below 4.0 keV. The total, **gaussian** component, and **simpl*diskbb** component are shown as the thick solid, thin dotted, and thin dash-dotted lines, respectively. To account for the cross-normalization terms (see Table 5), the *NICER* data are divided by 0.901. *Bottom:* The ratio of data to the best-fit model. The y-axis is shown in linear scale from 0.7 to 1.3, and in log scale from 1.3 to 50. The data have been rebinned for visual clarity.

only include upscattering. The **gaussian** component was added to account for the existence of a relativistic broadened iron line, and we fixed the line center (E_{line}) at 6.4 keV. We fitted the *NICER* data over the 2.5–9.0 keV range. For HEG and MEG, we included the 0.8–10 keV and 0.4–7.0 keV bands, respectively. All data were fitted using χ^2 -statistics. The best-fit model is shown in Figure 11. The model parameters are given in Table 5.

As can be seen from the bottom panel of Figure 11, the model underpredicts the MEG data below ~ 0.8 keV. The MEG effective area below 1 keV is sensitive to the correction for contamination, which currently undercorrects for the increasing depth of the contaminant. The magnitude of the effect is estimated to be about 20% at 0.65 keV and 10% at 0.8 keV, in the sense that estimated MEG fluxes should be even larger than shown in Figure 11.

The HETGS data can be used to constrain N_{H} . By fitting a simple model to a limited wavelength range, the Mg I and Ne I edges due to the ISM can be determined directly. The continuum model in this case is empirical, a log-parabolic shape, and the edge is modeled in *isis*

(Houck & Denicola 2000) using the *edge* model, which has no structure at the edge but has the appropriate asymptotic behavior for the ISM edge. Fitting the 11–17 Å (0.73–1.13 keV) region, we find that the Ne I edge optical depth is $0.170^{+0.06}_{-0.07}$, giving an estimate of $N_{\text{H}} = 2.2^{+0.7}_{-0.9} \times 10^{21} \text{ cm}^{-2}$ (Wilms et al. 2000). An optical depth at the Ne I edge of 0.33 is expected when $N_{\text{H}} = 4.2 \times 10^{21} \text{ cm}^{-2}$, which is ruled out at the 4.3σ level. An independent measurement from fitting the Mg I line in the 8–11 Å (1.13–1.55 keV) region gives an optical depth of $0.043^{+0.021}_{-0.014}$, and $N_{\text{H}} = 3.1^{+1.5}_{-1.0} \times 10^{21} \text{ cm}^{-2}$.

Paper II measured the equivalent width (EW) of Na I D line and diffuse interstellar bands (DIBs) from a summed optical spectrum, and constrained the line-of-sight extinction to be $0.8 \lesssim E(B - V) \lesssim 1.2$. Using the calibration of $N_{\text{H}} = 5.55 \times 10^{21} \times E(B - V)$ (Predehl & Schmitt 1995), the line-of-sight column density can be inferred to be $4.4 < N_{\text{H}} / (10^{21} \text{ cm}^{-2}) < 6.7$. This is consistent with the N_{H} derived from the continuum fit. Therefore, in the *NICER*-only spectral analysis (Section 4.4), we adopt $N_{\text{H}} = 5 \times 10^{21} \text{ cm}^{-2}$.

4.4. *NICER*-only Spectral Analysis

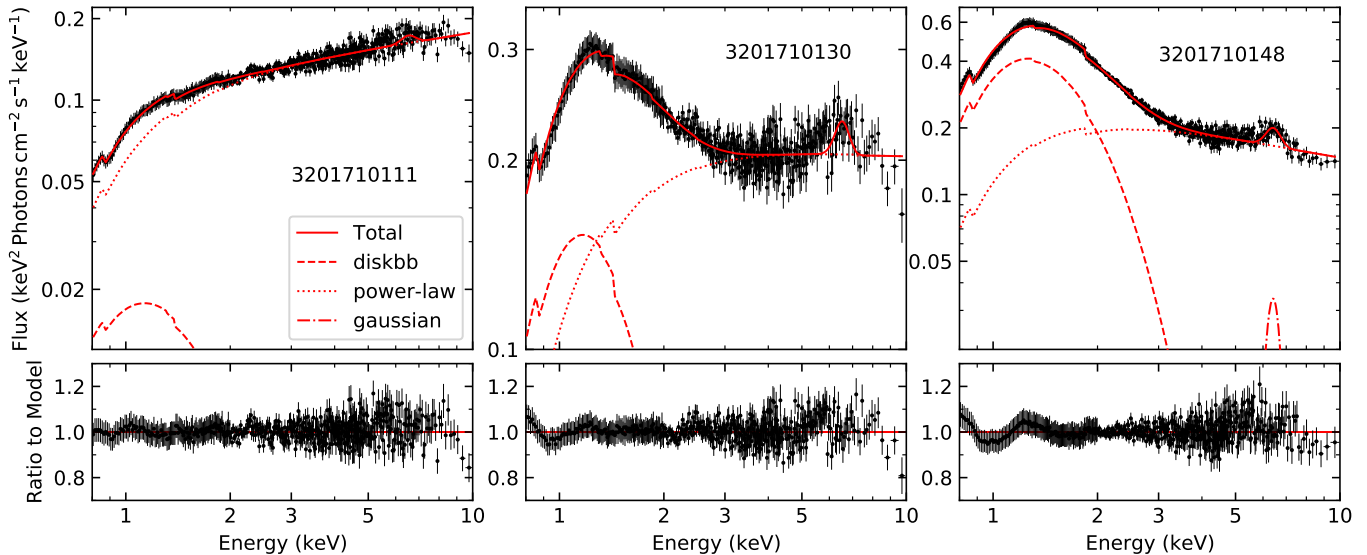


Figure 12. *NICER* spectral fitting at three representative epochs, OBSID 3201710111, 3201710130, and 3201710148. The total flux in the best-fit model is shown as solid lines. The flux contribution from the `diskbb`, `pegpwlw`, and `gaussian` components is shown as dashed, dotted, and dash-dotted lines, respectively.

Figure 12 shows the *NICER* spectra at three representative epochs (59076, 59100, and 59113 MJD). The continuum can be described by a combination of a multi-color disk component, a power-law component, and a Gaussian line component at 6.3–6.5 keV. To investigate the evolution of spectral components, for each OBSID, we fitted a `tbfeo*(diskbb+pegpwlw+gaussian)*edge` model to the 0.8–10 keV *NICER* spectrum. The `edge` feature at ≈ 1.4 keV was included, as found to be present in the *NICER* and *NuSTAR* joint spectral analysis (Section 4.2). In the `tbfeo` model, the O and Fe abundances were fixed at Solar values, and N_{H} was fixed at $5 \times 10^{21} \text{ cm}^{-2}$. All data were fitted using χ^2 -statistics. The best-fit models provided a reduced- χ^2 close to 1 in most of the cases.

The evolution of spectral parameters of the hydrogen column density N_{H} , the power-law photon index Γ , the temperature at inner disk radius T_{disk} , and the disk-blackbody normalization term $\text{Norm}_{\text{disk}} = (R_{\text{in}}/D_{10})^2 \cos i$ are shown in Figure 13. $\text{Norm}_{\text{disk}}$ remained almost constant after 59082 MJD. This provides evidence that the inner disk radius (R_{in}) remained at ~ 100 – 1000 km assuming a range of distances from $D \sim 10$ kpc to 1 kpc.

In the bottom panel of Figure 13, we present the unabsorbed 0.4–10 keV fluxes in the disk-blackbody component, the power-law component, and the total (disk-blackbody + power-law + Gaussian). Note that the Fe line flux is significantly smaller than the other two components. The occasional enhancement observed in

the source light curve matches to the brightening of the thermal component.

5. DISCUSSION

5.1. X-ray States in AT2019wey

The X-ray spectral-timing properties of AT2019wey are in line with the typical properties of LMXBs in the LHS and HIMS.

From 2019 December to 59082 MJD (2020 August 21), AT2019wey stayed in the canonical LHS of LMXBs. In the first six months, the spectrum was dominated by a hard power-law component ($1.7 \lesssim \Gamma \lesssim 2.0$) with little contribution from the disk component (Figures 9 and 13). It moved along the HL on the RID (Figure 5), and the fractional rms stayed at $\sim 30\%$. No QPO was observed (Section 3.2). The X-ray color softened as the source brightened (Figure 3). Toward the end of the brightening, spectral features of relativistic reflection were clearly seen (Figure 10). Modeling of the reflection spectrum suggests a small inclination ($i \lesssim 30^\circ$, see Appendix B.3). The rms variability decreased with increasing photon energy (right panel of Figure 8), indicating that cooler regions of the source are more variable than hotter regions, perhaps due to inhomogeneities in an accretion disk.

Between 59082 MJD and 59122 MJD (2020 September 30), AT2019wey was in the canonical HIMS of LMXBs. The power-law component steepened ($2.0 \lesssim \Gamma \lesssim 2.3$), and the thermal disk emission became comparable to the power-law component in the 0.4–10 keV band (Figure 13). The excess in the very soft X-ray band (Sec-

Table 4. Best-fit model parameters of the 2020 August 16 joint observations.

Parameter	90% Interval
constant	
$\mathcal{C}_{\text{FPMA}}$	1 (frozen)
$\mathcal{C}_{\text{FPMB}}$	1.051 ± 0.003
$\mathcal{C}_{\text{NICER}}$	1.035 ± 0.002
tbfeo	
N_{H} (10^{22} cm $^{-2}$)	0.513 ± 0.003
O	< 0.020
Fe	< 0.0528
z	0 (frozen)
simplcutx	
Γ	1.786 ± 0.001
f_{sc}	0.746 ± 0.005
R_{F}	1 (frozen)
kT_e (keV)	1000 (frozen)
diskbb	
T_{disk} (keV)	0.3542 ± 0.0001
R_{in}^* †	40.58 ± 0.03
relxillCp	
q	3 (frozen)
a	0 (frozen)
i (deg)	$27.0^{+0.8}_{-1.2}$
R_{in} (R_{isco})	< 1.05
R_{out} (R_{g})	400 (frozen)
$\log \xi$	$3.0121^{+0.0016}_{-0.0020}$
A_{Fe}	$2.86^{+0.10}_{-0.09}$
kT_e (keV)	1000 (frozen)
R_{F}	1 (frozen)
Norm_{rel} (10^{-4})	2.96 ± 0.03
edge	
E_c (keV)	$1.369^{+0.017}_{-0.016}$
D	$0.071^{+0.005}_{-0.005}$
C-stat / d.o.f.	2006.52 (1769)

† Normalization $(R_{\text{in}}/D_{10})\sqrt{\cos i}$, where R_{in} is the inner disk radius in the unit of km, and D_{10} is distance to the source in units of 10 kpc.

tion 4.3) might arise from reprocessing of X-rays in the outer accretion disk. Its soft X-ray light curve underwent a few episodes of mini-outbursts, which were correlated with the enhancement of a thermal component. At the same time, the source left the HL on the RID as the fractional rms decreased (Figure 5). A weak type-C LFQPO was observed, and its characteristic frequency increased from ~ 2 Hz to ~ 6.5 Hz as the disk flux in-

Table 5. Best-fit model parameters of the 2020 September 20 joint observations.

Parameter	90% Interval
constant	
$\mathcal{C}_{\text{HETG}}$	1 (frozen)
$\mathcal{C}_{\text{NICER}}$	0.901 ± 0.007
tbabs	
N_{H} (10^{22} cm $^{-2}$)	$0.417^{+0.014}_{-0.013}$
simpl	
Γ	2.80 ± 0.05
f_{sc}	0.176 ± 0.007
R_{up}	1 (fixed)
diskbb	
T_{disk} (keV)	$0.315^{+0.004}_{-0.005}$
R_{in}^* †	136 ± 6
gaussian	
E_{line} (keV)	6.4 (fixed)
σ_{line} (keV)	1.84 ± 0.09
$\text{Norm}_{\text{line}}^{\ddagger}$	0.0074 ± 0.0007
$\chi^2 / \text{d.o.f.}$	12095.94 (23735)

† R_{in}^* has the same meaning as that in Table 4.

‡ Normalization of the Gaussian in photon cm $^{-2}$ s $^{-1}$.

creased. It did not reach the SIMS since the fractional rms was $> 9\%$ at the minimum (Figure 4).

AT2019wey likely stayed in the HIMS from 2020 October 1 to November 30, since the 2–10 keV and 15–50 keV light curves remained roughly constant (Figure 1). We note that after being active in X-ray for at least ~ 12 months, AT2019wey had not transitioned to the SIMS or HSS. The lack of hysteresis in the HID (Figure 3) is similar to the BH candidate MAXI J1836–194 (Russell et al. 2013).

Paper II reported the radio brightening as AT2019wey transitioned from LHS to HIMS. Yadlapalli et al. (2021) reported the detection of a resolved radio source during the HIMS, which was interpreted as a steady compact jet. The evolution of the radio emission is consistent with LMXBs in the hard states (Fender et al. 2004; Migliari & Fender 2006).

The X-ray properties observed in AT2019wey thus far make it a promising candidate for the population of “hard-only” outbursts (Tetarenko et al. 2016). The distance of this system is poorly constrained to ~ 1 –10 kpc (Paper II). Given the brightness of AT2019wey in the optical ($r \approx 17.4$ mag), the *Gaia* mission will be able to determine the parallax to the source and thus settle the

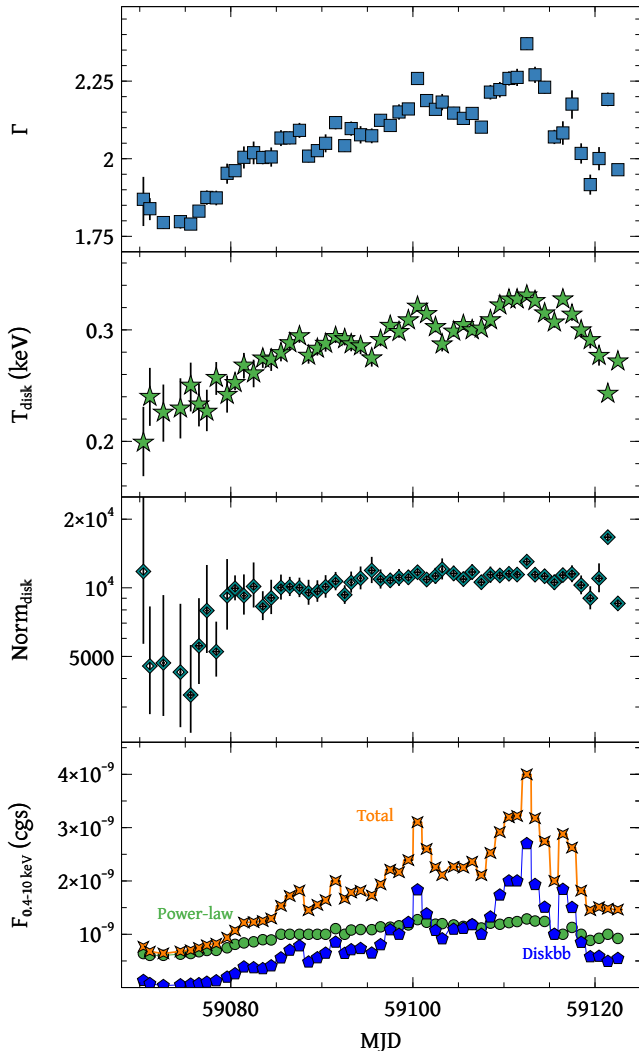


Figure 13. Evolution of *NICER* spectral best-fit parameters, and unabsorbed 0.4–10 keV flux from the `diskbb` component (blue pentagons), the `pegpwlw` component (green circles), and the total (orange crosses).

distance. Assuming a typical distance at 3–5 kpc, the 0.3–100 keV X-ray luminosity of AT2019wey remained at a few times 10^{35} erg s $^{-1}$ (Section 4.1) for ~ 6 months in the LHS, increased by a factor of ~ 10 to a few times 10^{36} erg s $^{-1}$ (Section 4.2) over ~ 2 months, and stayed at this luminosity afterward in the HIMS. This range of X-ray luminosities is at the lower end of the whole population of BH transients, but is typical for “hard-only” outbursts (Tetarenko et al. 2016).

5.2. Nature of the Compact Object

NS signatures of coherent pulsations and thermonuclear X-ray bursts were not detected in 394 ks of *NICER* and 80 ks of *NuSTAR* data (see Appendix B). The X-

ray spectral and timing properties shown in this paper are consistent with both NS and BH LMXB outbursts. However, a few properties of this source favor a BH accretor.

First of all, during the initial six months of the LHS, the power-law index was $\Gamma \approx 1.77$ and the 0.5–10 keV luminosity was 4.5×10^{33} – 4.5×10^{35} erg s $^{-1}$ (Section 4.1). This makes AT2019wey closer to BH binaries on the Γ – L_X diagram (see Fig. 2 of Wijnands et al. 2015). Moreover, the positions of this source on the L_{radio} – L_X and the L_{opt} – L_X diagrams are also closer to BH binaries (Paper II).

Therefore, although we can not preclude the possibility of a NS at this time, it is highly suggestive that AT2019wey is a BH system.

5.3. The Slow Rise of the Outburst

LMXB outbursts (also termed as X-ray novae) span a wide range of morphological types (Chen et al. 1997). Theories for the canonical fast-rise exponential-decay (FRED) profile of X-ray novae have been developed based on the disk instability model (DIM), which was originally invoked to explain dwarf nova outbursts (Lasota 2001). Disk truncation and irradiation are generally invoked to account for the longer evolution timescale and recurrence time of X-ray novae (van Paradijs 1996; Dubus et al. 2001). Recently, detailed analysis of the decay profile of X-ray outbursts provides evidence for the existence of generic outflows and time-varying irradiation (Tetarenko et al. 2018b,a; Shaw et al. 2019; Tetarenko et al. 2020).

Here we focus on the rise profile of AT2019wey. Paper II shows that the orbital period of AT2019wey is likely less than 16 hours. To compare AT2019wey with other short-period LMXBs, we select outbursts discovered between 2009 and 2020 from the BlackCAT⁶ catalog (Corral-Santana et al. 2016). Systems with $P_{\text{orb}} \lesssim 16$ hours are summarized in Table 6. Figure 14 shows their *MAXI* 2–10 keV light curves. We excluded IGR J17451–3022 since its *MAXI* data was highly contaminated by the bright persistent source 1A 1742–294. We also excluded the 2017 and 2019 outbursts of Swift J1357.2–0933 since their X-ray fluxes were too faint to be seen by *MAXI*—they were only detected by follow-up observations conducted by *NuSTAR*, *Swift*/XRT, and *NICER* (Beri et al. 2019a,b; Gandhi et al. 2019; Rao et al. 2019).

Figure 14 (middle and right panels) show that the 2–10 keV light curves of MAXI J1305–704,

⁶ <http://www.astro.puc.cl/BlackCAT/index.php>

Table 6. Short-period ($P_{\text{orb}} < 16$ hr) BH or BH candidate LMXB outbursts discovered from 2009 to 2020.

Name	P_{orb} (hr)	Discovery Instrument	Discovery Date	X-ray States	References
AT2019wey	< 16	ATLAS; <i>SRG</i>	2019 Dec 7	LHS, HIMS	1, 2, 23, 24
MAXI J1305–704	9.7	<i>MAXI</i>	2012 Apr 9	IMS	3, 4, 5, 25
Swift J1357.2–0933	2.8	<i>Swift</i> /BAT	2011 Jan 28	LHS	6, 7, 8
		CRTS	2017 Apr 20	LHS	9, 10
		ZTF	2019 Mar 31	–	11
MAXI 1659–152	2.4	<i>Swift</i> /BAT, <i>MAXI</i>	2010 Sep 25	LHS, IMS, HSS	5, 12, 13, 14
IGR J17451–3022	6.3	<i>INTEGRAL</i>	2014 Aug 22–24	HSS	20, 21, 22
XTE J1752–223	< 6.8	<i>RXTE</i>	2009 Oct 23	LHS, IMS, HSS	5, 15, 16
MAXI 1836–194	< 4.9	<i>MAXI</i> , <i>Swift</i> /BAT	2011 Aug 30	LHS, HIMS	17, 18, 19

NOTE— Instruments: the International Gamma-Ray Astrophysics Laboratory (*INTEGRAL*; Winkler et al. 2003); the Rossi X-ray Timing Explorer (*RXTE*; Swank 1999); the Catalina Real-Time Transient Survey (CRTS; Drake et al. 2009); the Zwicky Transient Facility (ZTF; Bellm et al. 2019; Graham et al. 2019). References. (1) This work (2) Paper II (3) Sato et al. (2012) (4) Shidatsu et al. (2013) (5) Tetarenko et al. (2016) (6) Krimm et al. (2011) (7) Corral-Santana et al. (2013) (8) Armas Padilla et al. (2013) (9) Drake et al. (2017) (10) Beri et al. (2019a) (11) van Velzen et al. (2019) (12) Negoro et al. (2010) (13) Mangano et al. (2010) (14) Kuulkers et al. (2013) (15) Markwardt et al. (2009) (16) Ratti et al. (2012) (17) Negoro et al. (2011) (18) Ferrigno et al. (2012) (19) Russell et al. (2014) (20) Chenevez et al. (2014) (21) Jaisawal et al. (2015) (22) Bozzo et al. (2016) (23) Tonry et al. (2019) (24) Mereminskiy et al. (2020) (25) Morihana et al. (2013)

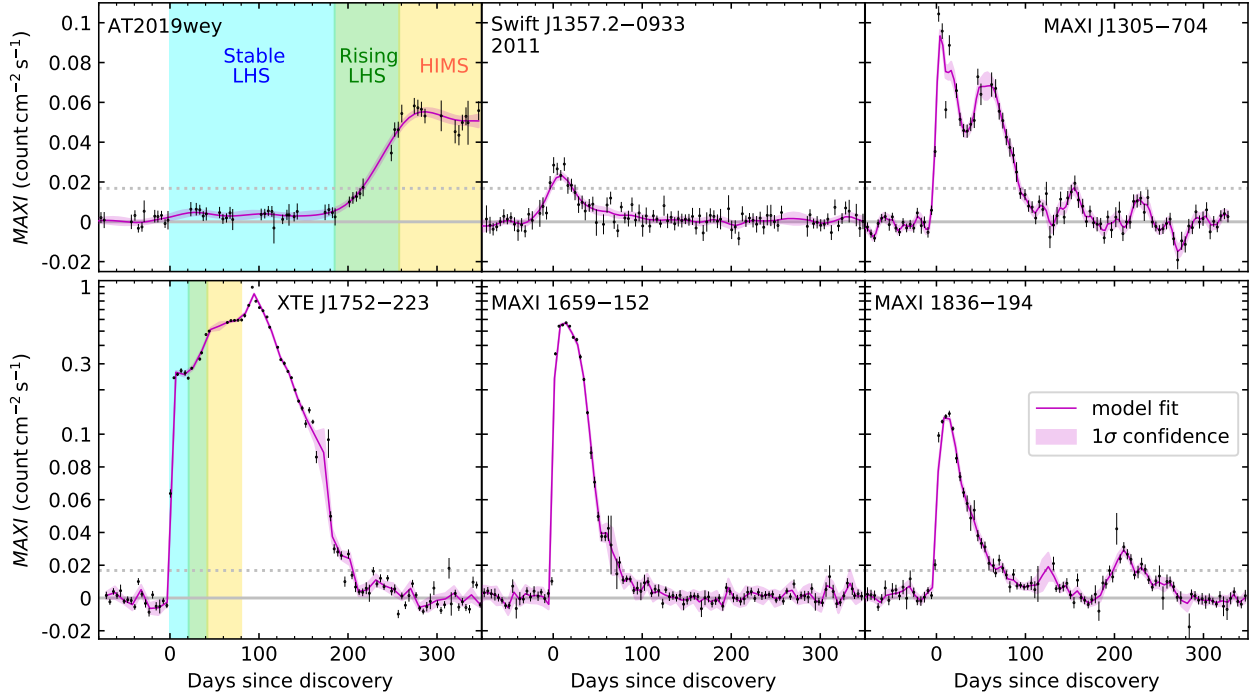


Figure 14. *MAXI* 2–10 keV Light curves of outbursts from short-period systems. The background of AT2019wey and XTE J1752–223 are color-coded to emphasize the two stable flux levels during the LHS and HIMS. In each panel, the black data points are 4-day binned light curves. The magenta curve is a model fit to the data, generated with a Gaussian process following procedures outlined in Appendix B.4 of Yao et al. (2020d). The dotted horizontal line marks *MAXI* 4 day 3σ detection limit of 7 mCrab in the 3–10 keV band (Negoro et al. 2016). The y-axis is shown in linear scale below 0.1, and in log scale above 0.1. The light curves of MAXI J1305–704 and XTE J1752–223 are affected by leak counts from nearby bright sources periodically due to the 72 days ISS orbital precessions. We have subtracted the average count rate between 2015 and 2020 to remove first-order contamination.

MAXI J1659–152, MAXI J1836–194, and the 2011 outburst of Swift J1357.2–0933 rose to maximum in 5–20 days. In comparison, the evolution of AT2019wey’s light curve (upper left panel of Figure 14) is rather slow. Its 2–10 keV flux rose to ~ 1 mCrab upon discovery, remained at this level for about 6 months, and brightened to a maximum of only ~ 20 mCrab afterwards. This is similar to the initial evolution of XTE J1752–223 (lower left panel of Figure 14), where the source stayed in the hard state with two stable flux levels for about 3 months (Nakahira et al. 2010)⁷. In the left panels of Figure 14, we color-code the background of the two stable flux levels by blue and yellow, and the rising between the two stable levels by green. As mentioned by Nakahira et al. (2010), the long duration of the initial LHS and the two plateau phases are rather uncommon for recorded LMXB outbursts, and might be accounted for by a slow increase of \dot{M} . We note that XTE J1752–223 later transitioned to the HSS and completed the hysteresis pattern on the HID. It remains to be seen if AT2019wey will transition to the HSS.

6. CONCLUSION

In this paper, we present *NICER*, *NuSTAR*, *Chandra*, *Swift*, and *MAXI* observations of the X-ray transient AT2019wey (SRGA J043520.9+552226, SRGE J043523.3+552234). By analyzing its spectral-timing properties, we conclude that AT2019wey is a LMXB outburst with a BH or NS accretor. The source’s evolution from 2019 December to 2020 November can be separated by three phases: the stable LHS from 2019 December to 2020 May (~ 1 mCrab), the rising LHS from 2020 June to August, and the stable HIMS from 2020 August to November (~ 20 mCrab).

The long duration of the initial LHS and the two plateau phases of AT2019wey (Figure 14) are not commonly seen. We searched the literature for analogs of AT2019wey. The closest analog we found is XTE J1752–223, a candidate BH LMXB with an orbital period of < 7 hr (Table 6).

If *SRG* had not discovered AT2019wey in 2020 March, the source would have probably been discovered by *MAXI* or *BAT* during the HIMS, and in a retrospective fashion, the initial ~ 1 mCrab flux excess could have been revealed by *MAXI* long-term monitoring. However, the *SRG* discovery is important to trigger rapid X-ray follow-up observations, which classify the initial plateau phase as in the LHS.

The repeated *SRG* all-sky surveys that are being carried offer the opportunity to discover other events similar to AT2019wey at early epochs (and thus enable critical multi-wavelength follow-up). Furthermore, the eROSITA sensitivity is unprecedented: $< 5 \times 10^{-14}$ erg s⁻¹ cm⁻² (1.3 μ Crab) in the 0.3–2.2 keV band, and $< 7 \times 10^{-13}$ erg s⁻¹ cm⁻² (36 μ Crab) in the 2.3–8 keV band (Predehl et al. 2021). This sensitivity should lead to the discovery of fainter versions of AT2019wey look-alikes.

1 We thank the anonymous reviewer for providing com-
 2 ments that have largely improved this manuscript. We
 3 thank Belinda Wilkes and Patrick Slane for allocat-
 4 ing DD time on *Chandra*, and Fiona Harrison for al-
 5 locating *NuSTAR* DD time. We thank Kumiko Mori-
 6 hana for providing the cleaned *MAXI* light curve of
 7 MAXI J1305–704. Y.Y. thanks the Heising–Simons
 8 Foundation for support. R.M.L. acknowledges the sup-
 9 port of NASA through Hubble Fellowship Program
 10 grant HST-HF2-51440.001. J.A.G. acknowledges sup-
 11 port from NASA grant 80NSSC17K0515 and from the
 12 Alexander von Humboldt Foundation. Z.W. acknowl-
 13 edges support from the NASA postdoctoral program.
 14 *NICER* research at NRL is supported by NASA. This
 15 work was partially supported under NASA contract No.
 16 NNG08FD60C and made use of data from the *NuS-*
 17 *TAR* mission, a project led by the California Institute of
 18 Technology, managed by the Jet Propulsion Laboratory,
 19 and funded by the National Aeronautics and Space Ad-
 20 ministration. We thank the *NuSTAR* Operations, Soft-
 21 ware, and Calibration teams for support with the exe-
 22 cution and analysis of these observations. This research
 23 has made use of the *NuSTAR* Data Analysis Software
 24 (*nustardas*), jointly developed by the ASI Science Data
 25 Center (ASDC, Italy) and the California Institute of
 26 Technology (USA). This work made use of data supplied
 27 by the UK *Swift* Science Data Centre at the University
 28 of Leicester.

Software: *astropy* (Astropy Collaboration et al. 2013), *CIAO* (Fruscione et al. 2006), *HEASoFT* (v6.27; Heasarc 2014), *HENDRICS* (Bachetti 2015), *isis* (Houck & Denicola 2000), *matplotlib* (Hunter 2007), *pandas* (McKinney 2010), *PRESTO* (Ransom 2011); *relxill* (v1.3.10; García et al. 2014; Dauser et al. 2014) *Stingray* (Huppenkothen et al. 2019), *xspec* (v12.11.0; Arnaud 1996)

Facilities: *NICER*, *NuSTAR*, *CXO* (ACIS-S), *Swift* (XRT, BAT), *MAXI*

APPENDIX

A. OBSERVATION LOGS

Here we present observation logs of *NICER* (Table 7), *NuSTAR* (Table 8), and *Swift*/XRT (Table 9).

B. DETAILS OF ANALYSIS

B.1. *NICER* Pulsation Search

Pulsation searches were carried out for all *NICER* data presented in Table 7. The *NICER* data contains 2257 GTIs spread over 394 ks of observations. Upon cursory inspection of the data with `NICERsoft`⁸, we found that detectors 34 and 43 suffered from high optical loading. Thus, the events in these detectors were excluded. The events were barycentered using `barycorr`. We employed acceleration search and stacked power spectral search schemes to search for pulsations.

To start with, we searched for pulsations using acceleration search. To account for possible frequency shifts due to binary Doppler motion, we employed an acceleration search algorithm over the f - \dot{f} plane in the Pulsar Exploration and Search TOolkit (`PRESTO`⁹; Ransom 2011). The acceleration search is valid under the assumption that the pulsar has a constant acceleration throughout the observation, and is most effective for observation durations of $T \lesssim P_{\text{orb}}/10$ (Ransom et al. 2002).

To determine the GTIs (and hence event files) used in the acceleration searches, we started from the 2257 GTIs in the original filtered event file. In order to prevent very short GTIs from being used, adjacent GTIs that were less than 11 s apart were combined. This resulted in a total of 445 GTIs, ranging in length from 1 s to 2648 s. We imposed a minimum GTI duration of 64 s to avoid spurious signals in short GTIs, leaving 378 GTIs with a median length of 883 s. For each of these GTIs (considered independently), we further filtered events from three energy ranges: 0.5–2 keV, 2–12 keV, and 0.5–12 keV. The 1134 event files were then extracted with `niextract-events`. We then ran the

search using the `accelsearch` task in `PRESTO` over the range 1–1000 Hz, positing that Doppler shifting would cause the possible signal to drift across a maximum of 100 Fourier frequency bins. For the median GTI length (883 s) and a fiducial fundamental pulsation frequency of 300 Hz, this corresponds to accelerations of up to $a = z_{\text{max}}c/(fT^2) \approx 130 \text{ m s}^{-2}$. The typical acceleration in a NS LXMB, say in a 12-hour orbit around a $0.2 M_{\odot}$ companion, is approximately 5.7 m s^{-2} . The acceleration searches yielded no candidate signals above the statistical significance threshold of $3\text{-}\sigma$, after accounting for the total number of trials.

An alternative pulsation search algorithm involves stacking power spectra from M segments and calculating an averaged power spectrum. This is Bartlett’s method (Bartlett 1948), in which the original time series is broken up into M non-overlapping segments of equal length. The M segments were binned at $\Delta t = 0.5$ ms, such that we sampled at the Nyquist frequency of 1000 Hz. The Leahy-normalized power spectrum was then computed for each of the M segments, using the `realfft` task in `PRESTO` (Leahy et al. 1983). Finally, the M resulting spectra were averaged and the corresponding noise distributions were calculated. The detection level for any candidate signal was then determined by calculating the probability that the power in any frequency bin exceeded that of a detection threshold (say, $3\text{-}\sigma$). This was calculated through the integrated probability of the χ^2 distribution with $2MW$ degrees of freedom, with W being the rebinning factor (van der Klis 1988). The stacking procedure was done to enhance the signal of faint millisecond pulsars.

The stacked power spectra were calculated with segments of length 64, 128, 256, and 512 s, to account for possible orbital modulations in the pulsar frequency with yet unknown binary parameters. On top of stacking the power spectra from segments of the entire time series, the stacked power spectra were also calculated for various sub-time series, where the choices were informed by the overall light curve binned at 128 s and looking at the source brightness level. The number of segments admitted into the calculation for the stacked power spectrum also depends on a segment threshold (in %). That is, for each segment, a 1-s binned light curve was generated. If the fraction of bins with counts is less than the threshold, then that segment will not be used in the calculation. Segment thresholds used were 20%, 50%, 70%, and 100%. We also searched over energy ranges 0.5–2 keV, 2–12 keV, and 0.5–12 keV. The aver-

⁷ The exact time of the LHS \rightarrow HIMS transition was not well determined for XTE J1752–223 (Brocksopp et al. 2013).

⁸ <https://github.com/paulray/NICERsoft>

⁹ <https://www.cv.nrao.edu/~sransom/presto/>

Table 7. *NICER* Observation Log

OBSID	Exp.	Start Time	OBSID	Exp.	Start Time	OBSID	Exp.	Start Time
	(ks)	(UT)		(ks)	(UT)		(ks)	(UT)
3201710105	0.22	2020-08-09 08:28	3201710106	1.10	2020-08-10 01:30	3201710107	4.82	2020-08-11 09:59
3201710108	6.02	2020-08-12 07:43	3201710109	4.39	2020-08-13 08:30	3201710110	8.00	2020-08-14 04:38
3201710111	10.55	2020-08-15 00:54	3201710112	4.21	2020-08-16 03:01	3201710113	4.85	2020-08-17 00:43
3201710114	2.52	2020-08-18 13:52	3201710115	7.41	2020-08-19 02:14	3201710116	3.15	2020-08-20 04:51
3201710117	2.32	2020-08-21 02:37	3201710118	6.39	2020-08-22 02:07	3201710119	3.57	2020-08-23 00:59
3201710120	5.87	2020-08-24 00:25	3201710121	8.95	2020-08-24 23:36	3201710122	7.58	2020-08-26 03:29
3201710123	7.76	2020-08-27 02:43	3201710124	10.07	2020-08-28 00:25	3201710125	3.65	2020-08-29 01:12
3201710126	6.54	2020-08-30 00:26	3201710127	7.99	2020-08-31 02:49	3201710128	4.84	2020-09-01 00:31
3201710129	2.97	2020-09-02 01:18	3201710130	3.71	2020-09-03 00:31	3201710131	6.90	2020-09-04 01:18
3201710132	8.44	2020-09-05 00:32	3201710133	5.43	2020-09-06 02:46	3201710134	12.36	2020-09-07 00:05
3201710135	13.69	2020-09-08 01:08	3201710136	23.53	2020-09-09 00:29	3201710137	14.38	2020-09-10 01:13
3201710138	5.67	2020-09-11 01:47	3201710139	8.76	2020-09-11 23:34	3201710140	11.32	2020-09-13 03:34
3201710141	10.02	2020-09-14 02:35	3201710142	10.49	2020-09-15 02:07	3201710143	5.80	2020-09-16 02:51
3201710144	5.45	2020-09-17 03:40	3201710145	8.38	2020-09-18 02:58	3201710146	10.22	2020-09-19 00:12
3201710147	16.59	2020-09-20 01:03	3201710148	6.54	2020-09-21 00:13	3201710149	11.19	2020-09-21 23:27
3201710150	8.84	2020-09-23 03:24	3201710151	5.97	2020-09-24 01:02	3201710152	3.34	2020-09-25 01:52
3201710153	3.82	2020-09-26 01:06	3201710154	2.53	2020-09-27 01:52	3201710155	3.11	2020-09-28 01:06
3201710156	4.25	2020-09-29 00:20	3201710157	6.22	2020-09-30 01:10			

Table 8. *NuSTAR* Observation Log

OBSID	Exp.	Start Time	Count Rate
	(ks)	(UT)	(count s ⁻¹)
90601315002	38	2020-04-18 11:21	2.3 ± 0.7
90601315004	42	2020-08-16 12:16	30.8 ± 2.6
90601315006	37	2020-08-27 02:51	35.1 ± 2.7

aged power spectrum was finally calculated by dividing the total power spectrum by the number of segments used.

From all of these stacked power spectra, there were no candidate signals that exceeded the $3\text{-}\sigma$ detection level, after accounting for the total number of trials.

B.2. *NuSTAR* Pulsation Search

We used HENDRICS to perform the timing analysis. Initially developed as MaLTPyNT (Bachetti 2015) for timing analysis of *NuSTAR* data, HENDRICS now comprises of tools such as acceleration searches, periodograms, Z_n^2 statistics to search for pulsations and extends to some other X-ray missions (e.g., *NICER*). We began this analysis by first calibrating the datafile by using the re-

Table 9. *Swift*/XRT Observation Log

OBSID	Exp.	Start Time	Mode	Count Rate
	(s)	(UT)		(count s ⁻¹)
13313001	1523	2020-04-12 06:07	PC	0.645 ± 0.029
13313002	874	2020-04-17 19:55	PC	0.570 ± 0.035
13313003	1026	2020-04-24 14:28	PC	0.639 ± 0.036
13313004	1043	2020-04-28 13:56	PC	0.717 ± 0.051
13313010	434	2020-09-02 20:36	WT	27.57 ^{+0.28} _{-0.31}
13313011	1023	2020-09-09 16:40	WT	42.50 ^{+1.58} _{-1.54}
13313012	858	2020-09-16 16:01	WT	43.32 ^{+0.26} _{-0.29}
13313013	794	2020-09-23 20:03	WT	40.53 ^{+2.35} _{-2.27}

NOTE—Count rate is given in the 0.3–10 keV band.

sponse file for each observation and constructing the light curve using HENcalibrate. The intent here was to check if AT2019wey exhibited rapid variability along with modality such that the light curve could be distributed into ‘high’, ‘low’ and ‘flare’ regions as seen in transitional millisecond pulsars. No modality was observed.

Similar to the techniques used in Appendix B.1, we launched acceleration search using `PRESTO` to search for periodic pulsations. We split the observation into chunks of 720s each and allowed for 5% overlap within these chunks. We then used `HENbinary` from `Hendrics` to render these time series in the format preferred by `accelsearch`. We binned the light curve to 1 ms bins. After that, we used the `accelsearch` routine in `PRESTO` and searched to a `zmax` depth of 10 and detection threshold of 2σ . No viable “candidates” were detected.

B.3. Modeling Relativistic Reflection

Here we present details of the spectral fitting in Section 4.2.

In the `relxillCp` model, the Γ parameter (power law index of the incident spectrum) was fixed at the same value as that in the `simpcutx` model. The outer disk radius (R_{out}) was fixed at a fiducial value of $400 r_g$ (Choudhury et al. 2017), since it has little effect on the X-ray spectrum. Here $r_g = GM/c^2$ is the gravitational radius. The electron temperature (kT_e) describes the observed high energy cutoff of the spectrum. Since no sign of a power-law cutoff was observed in the *NuSTAR* data, kT_e was fixed at the maximum value of 1 MeV. Redshift (z) was fixed at 0 since AT2019wey is a Galactic source. We included a cross-normalization term (`constant`) between FPMA, FPMB, and *NICER* data. To reduce the

complexity of this model, we frozen the reflection fraction ($R_F = 1$). The inner and outer emissivity index were set at the same value q throughout the accretion disk, making R_{break} obsolete.

If we fix the black hole spin parameter at $a = 0$ or $a = 0.998$, and let R_{in} , q , and i be free, then the fitting will result in parameters loosely constrained, as most of these parameters are correlated (Dauser et al. 2013). Therefore, we experimented by fitting multiple models, and for each model we fixed two of the four parameters. First, we fixed $a = 0$, $q = 3$, and let R_{in} and i be free. The best-fit values are listed in Table 4.

Next, we fixed $a = 0.998$, the inclination to the value obtained in the previous fit ($i = 27.0^\circ$), and allowed R_{in} and q to be free. The best-fit model has similar statistics to that with $a = 0$ (Table 4). However, this model results in a flatter emissivity law ($q \sim 2.8$) with an inner radius still relatively close to ISCO ($R_{\text{in}} \sim 4 \pm 3 R_{\text{ISCO}}$). This is contrary to the theoretical expectation of a steep emissivity profile for rapidly rotating black holes with compact coronae, unless the source of power-law photons is placed much farther along the rotational axis, which conversely will result in weaker reflection features (see Fig. 3 in Dauser et al. 2013).

Finally, we fixed $a = 0$ or $a = 0.998$, and i to higher values (45° , 60°). The fit quality decreases, with clear residuals around the Fe line. Therefore, from the point of view of reflection, the inclination (i) of the inner disk is well constrained to $i \lesssim 30^\circ$.

REFERENCES

- Armas Padilla, M., Degenaar, N., Russell, D. M., & Wijnand s, R. 2013, *MNRAS*, 428, 3083, doi: [10.1093/mnras/sts255](https://doi.org/10.1093/mnras/sts255)
- Arnaud, K. A. 1996, in *Astronomical Society of the Pacific Conference Series*, Vol. 101, *Astronomical Data Analysis Software and Systems V*, ed. G. H. Jacoby & J. Barnes, 17
- Astropy Collaboration, Robitaille, T. P., Tollerud, E. J., et al. 2013, *A&A*, 558, A33, doi: [10.1051/0004-6361/201322068](https://doi.org/10.1051/0004-6361/201322068)
- Bachetti, M. 2015, *MaLTPyNT: Quick look timing analysis for NuSTAR data*. <http://ascl.net/1502.021>
- Bachetti, M., Harrison, F. A., Cook, R., et al. 2015, *ApJ*, 800, 109, doi: [10.1088/0004-637X/800/2/109](https://doi.org/10.1088/0004-637X/800/2/109)
- Bachetti, M., Markwardt, C. B., Grefenstette, B. W., et al. 2021, *ApJ*, 908, 184, doi: [10.3847/1538-4357/abd1d6](https://doi.org/10.3847/1538-4357/abd1d6)
- Banerjee, S., Gilfanov, M., Bhattacharyya, S., & Sunyaev, R. 2020, *MNRAS*, 498, 5353, doi: [10.1093/mnras/staa2788](https://doi.org/10.1093/mnras/staa2788)
- Bartlett, M. S. 1948, *Nature*, 161, 686, doi: [10.1038/161686a0](https://doi.org/10.1038/161686a0)
- Bellm, E. C., Kulkarni, S. R., Graham, M. J., et al. 2019, *PASP*, 131, 018002, doi: [10.1088/1538-3873/aaecbe](https://doi.org/10.1088/1538-3873/aaecbe)
- Belloni, T. 2010, *The Jet Paradigm*, Vol. 794, doi: [10.1007/978-3-540-76937-8](https://doi.org/10.1007/978-3-540-76937-8)
- Belloni, T., Colombo, A. P., Homan, J., Campana, S., & van der Klis, M. 2002a, *A&A*, 390, 199, doi: [10.1051/0004-6361:20020703](https://doi.org/10.1051/0004-6361:20020703)
- Belloni, T., & Hasinger, G. 1990, *A&A*, 227, L33
- Belloni, T., Homan, J., Casella, P., et al. 2005, *A&A*, 440, 207, doi: [10.1051/0004-6361:20042457](https://doi.org/10.1051/0004-6361:20042457)
- Belloni, T., Psaltis, D., & van der Klis, M. 2002b, *ApJ*, 572, 392, doi: [10.1086/340290](https://doi.org/10.1086/340290)
- Beri, A., Tetarenko, B. E., Bahramian, A., et al. 2019a, *MNRAS*, 485, 3064, doi: [10.1093/mnras/stz616](https://doi.org/10.1093/mnras/stz616)
- Beri, A., Wijnands, R., Russell, T., et al. 2019b, *The Astronomer’s Telegram*, 12816, 1

- Bhattacharyya, S. 2009, *Current Science*, 97, 804.
<http://www.jstor.org/stable/24112117>
- Bogdanov, S., Guillot, S., Ray, P. S., et al. 2019, *ApJL*, 887, L25, doi: [10.3847/2041-8213/ab53eb](https://doi.org/10.3847/2041-8213/ab53eb)
- Boller, T., Freyberg, M. J., Trümper, J., et al. 2016, *A&A*, 588, A103, doi: [10.1051/0004-6361/201525648](https://doi.org/10.1051/0004-6361/201525648)
- Bozzo, E., Pjanka, P., Romano, P., et al. 2016, *A&A*, 589, A42, doi: [10.1051/0004-6361/201527501](https://doi.org/10.1051/0004-6361/201527501)
- Brocksopp, C., Bandyopadhyay, R. M., & Fender, R. P. 2004, *NewA*, 9, 249, doi: [10.1016/j.newast.2003.11.002](https://doi.org/10.1016/j.newast.2003.11.002)
- Brocksopp, C., Corbel, S., Tzioumis, A., et al. 2013, *MNRAS*, 432, 931, doi: [10.1093/mnras/stt493](https://doi.org/10.1093/mnras/stt493)
- Burrows, D. N., Hill, J. E., Nousek, J. A., et al. 2005, *SSRv*, 120, 165, doi: [10.1007/s11214-005-5097-2](https://doi.org/10.1007/s11214-005-5097-2)
- Canizares, C. R., Davis, J. E., Dewey, D., et al. 2005, *PASP*, 117, 1144, doi: [10.1086/432898](https://doi.org/10.1086/432898)
- Capitanio, F., Belloni, T., Del Santo, M., & Ubertini, P. 2009, *MNRAS*, 398, 1194, doi: [10.1111/j.1365-2966.2009.15196.x](https://doi.org/10.1111/j.1365-2966.2009.15196.x)
- Casella, P., Belloni, T., & Stella, L. 2005, *ApJ*, 629, 403, doi: [10.1086/431174](https://doi.org/10.1086/431174)
- Cash, W. 1979, *ApJ*, 228, 939, doi: [10.1086/156922](https://doi.org/10.1086/156922)
- Chen, W., Shrader, C. R., & Livio, M. 1997, *ApJ*, 491, 312, doi: [10.1086/304921](https://doi.org/10.1086/304921)
- Chenevez, J., Vandbaek Kroer, L., Budtz-Jorgensen, C., et al. 2014, *The Astronomer's Telegram*, 6451, 1
- Choudhury, K., García, J. A., Steiner, J. F., & Bambi, C. 2017, *ApJ*, 851, 57, doi: [10.3847/1538-4357/aa9925](https://doi.org/10.3847/1538-4357/aa9925)
- Connors, R. M. T., García, J. A., Dauser, T., et al. 2020, *ApJ*, 892, 47, doi: [10.3847/1538-4357/ab7afc](https://doi.org/10.3847/1538-4357/ab7afc)
- Coriat, M., Fender, R. P., & Dubus, G. 2012, *MNRAS*, 424, 1991, doi: [10.1111/j.1365-2966.2012.21339.x](https://doi.org/10.1111/j.1365-2966.2012.21339.x)
- Corral-Santana, J. M., Casares, J., Muñoz-Darias, T., et al. 2016, *A&A*, 587, A61, doi: [10.1051/0004-6361/201527130](https://doi.org/10.1051/0004-6361/201527130)
- . 2013, *Science*, 339, 1048, doi: [10.1126/science.1228222](https://doi.org/10.1126/science.1228222)
- Dauser, T., Garcia, J., Parker, M. L., Fabian, A. C., & Wilms, J. 2014, *MNRAS*, 444, L100, doi: [10.1093/mnrasl/slu125](https://doi.org/10.1093/mnrasl/slu125)
- Dauser, T., Garcia, J., Wilms, J., et al. 2013, *MNRAS*, 430, 1694, doi: [10.1093/mnras/sts710](https://doi.org/10.1093/mnras/sts710)
- Done, C., & Gierliński, M. 2003, *MNRAS*, 342, 1041, doi: [10.1046/j.1365-8711.2003.06614.x](https://doi.org/10.1046/j.1365-8711.2003.06614.x)
- Done, C., Gierliński, M., & Kubota, A. 2007, *A&A Rv*, 15, 1, doi: [10.1007/s00159-007-0006-1](https://doi.org/10.1007/s00159-007-0006-1)
- Drake, A. J., Djorgovski, S. G., Mahabal, A. A., et al. 2017, *The Astronomer's Telegram*, 10297, 1
- Drake, A. J., Djorgovski, S. G., Mahabal, A., et al. 2009, *ApJ*, 696, 870, doi: [10.1088/0004-637X/696/1/870](https://doi.org/10.1088/0004-637X/696/1/870)
- Dubus, G., Hameury, J. M., & Lasota, J. P. 2001, *A&A*, 373, 251, doi: [10.1051/0004-6361:20010632](https://doi.org/10.1051/0004-6361:20010632)
- Evans, P. A., Beardmore, A. P., Page, K. L., et al. 2007, *A&A*, 469, 379, doi: [10.1051/0004-6361:20077530](https://doi.org/10.1051/0004-6361:20077530)
- . 2009, *MNRAS*, 397, 1177, doi: [10.1111/j.1365-2966.2009.14913.x](https://doi.org/10.1111/j.1365-2966.2009.14913.x)
- Fender, R. P., Belloni, T. M., & Gallo, E. 2004, *MNRAS*, 355, 1105, doi: [10.1111/j.1365-2966.2004.08384.x](https://doi.org/10.1111/j.1365-2966.2004.08384.x)
- Ferrigno, C., Bozzo, E., Del Santo, M., & Capitanio, F. 2012, *A&A*, 537, L7, doi: [10.1051/0004-6361/201118474](https://doi.org/10.1051/0004-6361/201118474)
- Fruscione, A., McDowell, J. C., Allen, G. E., et al. 2006, in *Society of Photo-Optical Instrumentation Engineers (SPIE) Conference Series*, Vol. 6270, Society of Photo-Optical Instrumentation Engineers (SPIE) Conference Series, ed. D. R. Silva & R. E. Doxsey, 62701V, doi: [10.1117/12.671760](https://doi.org/10.1117/12.671760)
- Gandhi, P., Paice, J. A., Gendreau, K., et al. 2019, *The Astronomer's Telegram*, 12801, 1
- García, J., Kallman, T. R., & Mushotzky, R. F. 2011, *ApJ*, 731, 131, doi: [10.1088/0004-637X/731/2/131](https://doi.org/10.1088/0004-637X/731/2/131)
- García, J., Dauser, T., Lohfink, A., et al. 2014, *ApJ*, 782, 76, doi: [10.1088/0004-637X/782/2/76](https://doi.org/10.1088/0004-637X/782/2/76)
- Garmire, G. P., Bautz, M. W., Ford, P. G., Nousek, J. A., & Ricker, George R., J. 2003, in *Society of Photo-Optical Instrumentation Engineers (SPIE) Conference Series*, Vol. 4851, X-Ray and Gamma-Ray Telescopes and Instruments for Astronomy., ed. J. E. Truemper & H. D. Tananbaum, 28–44, doi: [10.1117/12.461599](https://doi.org/10.1117/12.461599)
- Gehrels, N., Chincarini, G., Giommi, P., et al. 2004, *ApJ*, 611, 1005, doi: [10.1086/422091](https://doi.org/10.1086/422091)
- Gendreau, K. C., Arzoumanian, Z., Adkins, P. W., et al. 2016, in *Society of Photo-Optical Instrumentation Engineers (SPIE) Conference Series*, Vol. 9905, Space Telescopes and Instrumentation 2016: Ultraviolet to Gamma Ray, 99051H, doi: [10.1117/12.2231304](https://doi.org/10.1117/12.2231304)
- Gilfanov, M. 2010, *X-Ray Emission from Black-Hole Binaries*, ed. T. Belloni, Vol. 794, 17, doi: [10.1007/978-3-540-76937-8_2](https://doi.org/10.1007/978-3-540-76937-8_2)
- Gilfanov, M., Revnivtsev, M., & Molkov, S. 2003, *A&A*, 410, 217, doi: [10.1051/0004-6361:20031141](https://doi.org/10.1051/0004-6361:20031141)
- Graham, M. J., Kulkarni, S. R., Bellm, E. C., et al. 2019, *PASP*, 131, 078001, doi: [10.1088/1538-3873/ab006c](https://doi.org/10.1088/1538-3873/ab006c)
- Harrison, F. A., Craig, W. W., Christensen, F. E., et al. 2013, *ApJ*, 770, 103, doi: [10.1088/0004-637X/770/2/103](https://doi.org/10.1088/0004-637X/770/2/103)
- Hasinger, G., & van der Klis, M. 1989, *A&A*, 225, 79
- Heasarc. 2014, *HEASoft: Unified Release of FTOOLS and XANADU*. <http://ascl.net/1408.004>
- Homan, J., & Belloni, T. 2005, *Ap&SS*, 300, 107, doi: [10.1007/s10509-005-1197-4](https://doi.org/10.1007/s10509-005-1197-4)
- Hori, T., Shidatsu, M., Ueda, Y., et al. 2018, *ApJS*, 235, 7, doi: [10.3847/1538-4365/aaa89c](https://doi.org/10.3847/1538-4365/aaa89c)

- Houck, J. C., & Denicola, L. A. 2000, in *Astronomical Society of the Pacific Conference Series*, Vol. 216, *Astronomical Data Analysis Software and Systems IX*, ed. N. Manset, C. Veillet, & D. Crabtree, 591
- Hunter, J. D. 2007, *Computing In Science & Engineering*, 9, 90, doi: [10.1109/MCSE.2007.55](https://doi.org/10.1109/MCSE.2007.55)
- Huppenkothen, D., Bachetti, M., Stevens, A. L., et al. 2019, *ApJ*, 881, 39, doi: [10.3847/1538-4357/ab258d](https://doi.org/10.3847/1538-4357/ab258d)
- Ingram, A. R., & Motta, S. E. 2019, *NewAR*, 85, 101524, doi: [10.1016/j.newar.2020.101524](https://doi.org/10.1016/j.newar.2020.101524)
- Jaisawal, G. K., Homan, J., Naik, S., & Jonker, P. 2015, *The Astronomer's Telegram*, 7361, 1
- Kaastra, J. S., & Bleeker, J. A. M. 2016, *A&A*, 587, A151, doi: [10.1051/0004-6361/201527395](https://doi.org/10.1051/0004-6361/201527395)
- Klein-Wolt, M., & van der Klis, M. 2008, *ApJ*, 675, 1407, doi: [10.1086/525843](https://doi.org/10.1086/525843)
- Krimm, H. A., Barthelmy, S. D., Baumgartner, W., et al. 2011, *The Astronomer's Telegram*, 3138, 1
- Krimm, H. A., Holland, S. T., Corbet, R. H. D., et al. 2013, *ApJS*, 209, 14, doi: [10.1088/0067-0049/209/1/14](https://doi.org/10.1088/0067-0049/209/1/14)
- Kuulkers, E., Kouveliotou, C., Belloni, T., et al. 2013, *A&A*, 552, A32, doi: [10.1051/0004-6361/201219447](https://doi.org/10.1051/0004-6361/201219447)
- Lasota, J.-P. 2001, *NewAR*, 45, 449, doi: [10.1016/S1387-6473\(01\)00112-9](https://doi.org/10.1016/S1387-6473(01)00112-9)
- Leahy, D. A., Darbro, W., Elsner, R. F., et al. 1983, *ApJ*, 266, 160, doi: [10.1086/160766](https://doi.org/10.1086/160766)
- Lewin, W. H. G., van Paradijs, J., & Taam, R. E. 1993, *SSRv*, 62, 223, doi: [10.1007/BF00196124](https://doi.org/10.1007/BF00196124)
- Ludlam, R. M., Cackett, E. M., García, J. A., et al. 2020, *ApJ*, 895, 45, doi: [10.3847/1538-4357/ab89a6](https://doi.org/10.3847/1538-4357/ab89a6)
- Lyapin, A., Zaznobin, I., Khorungev, G., et al. 2020, *The Astronomer's Telegram*, 13576, 1
- Madsen, K. K., Beardmore, A. P., Forster, K., et al. 2017, *AJ*, 153, 2, doi: [10.3847/1538-3881/153/1/2](https://doi.org/10.3847/1538-3881/153/1/2)
- Mangano, V., Hoversten, E. A., Markwardt, C. B., et al. 2010, *GRB Coordinates Network*, 11296, 1
- Markert, T. H., Canizares, C. R., Dewey, D., et al. 1994, in *Society of Photo-Optical Instrumentation Engineers (SPIE) Conference Series*, Vol. 2280, *EUV, X-Ray, and Gamma-Ray Instrumentation for Astronomy V*, ed. O. H. Siegmund & J. V. Vallerga, 168–180, doi: [10.1117/12.186812](https://doi.org/10.1117/12.186812)
- Markwardt, C. B., Swank, J. H., Barthelmy, S. D., et al. 2009, *The Astronomer's Telegram*, 2258, 1
- Matsuoka, M., Kawasaki, K., Ueno, S., et al. 2009, *PASJ*, 61, 999, doi: [10.1093/pasj/61.5.999](https://doi.org/10.1093/pasj/61.5.999)
- McClintock, J. E., & Remillard, R. A. 2006, *Black hole binaries*, Vol. 39, 157–213
- McKinney, W. 2010, in *Proceedings of the 9th Python in Science Conference*, ed. S. van der Walt & J. Millman, 51 – 56
- Mereminskiy, I., Medvedev, P., Semena, A., et al. 2020, *The Astronomer's Telegram*, 13571, 1
- Migliari, S., & Fender, R. P. 2006, *MNRAS*, 366, 79, doi: [10.1111/j.1365-2966.2005.09777.x](https://doi.org/10.1111/j.1365-2966.2005.09777.x)
- Mihara, T., Nakajima, M., Sugizaki, M., et al. 2011, *PASJ*, 63, S623, doi: [10.1093/pasj/63.sp3.S623](https://doi.org/10.1093/pasj/63.sp3.S623)
- Mitsuda, K., Inoue, H., Koyama, K., et al. 1984, *PASJ*, 36, 741
- Morihana, K., Sugizaki, M., Nakahira, S., et al. 2013, *PASJ*, 65, L10, doi: [10.1093/pasj/65.5.L10](https://doi.org/10.1093/pasj/65.5.L10)
- Morii, M., Yamaoka, H., Mihara, T., Matsuoka, M., & Kawai, N. 2016, *PASJ*, 68, S11, doi: [10.1093/pasj/psw007](https://doi.org/10.1093/pasj/psw007)
- Motta, S., Muñoz-Darias, T., Casella, P., Belloni, T., & Homan, J. 2011, *MNRAS*, 418, 2292, doi: [10.1111/j.1365-2966.2011.19566.x](https://doi.org/10.1111/j.1365-2966.2011.19566.x)
- Muñoz-Darias, T., Fender, R. P., Motta, S. E., & Belloni, T. M. 2014, *MNRAS*, 443, 3270, doi: [10.1093/mnr/stu1334](https://doi.org/10.1093/mnr/stu1334)
- Muñoz-Darias, T., Motta, S., & Belloni, T. M. 2011, *MNRAS*, 410, 679, doi: [10.1111/j.1365-2966.2010.17476.x](https://doi.org/10.1111/j.1365-2966.2010.17476.x)
- Nakahira, S., Yamaoka, K., Sugizaki, M., et al. 2010, *PASJ*, 62, L27, doi: [10.1093/pasj/62.5.L27](https://doi.org/10.1093/pasj/62.5.L27)
- Negoro, H., Yamaoka, K., Nakahira, S., et al. 2010, *The Astronomer's Telegram*, 2873, 1
- Negoro, H., Nakajima, M., Nakahira, S., et al. 2011, *The Astronomer's Telegram*, 3611, 1
- Negoro, H., Kohama, M., Serino, M., et al. 2016, *PASJ*, 68, S1, doi: [10.1093/pasj/psw016](https://doi.org/10.1093/pasj/psw016)
- Negoro, H., Nakajima, M., Aoki, M., et al. 2020, *The Astronomer's Telegram*, 13948, 1
- Pavlinsky, M., Tkachenko, A., Levin, V., et al. 2021, *A&A*, 650, A42, doi: [10.1051/0004-6361/202040265](https://doi.org/10.1051/0004-6361/202040265)
- Predehl, P., & Schmitt, J. H. M. M. 1995, *A&A*, 500, 459
- Predehl, P., Andritschke, R., Arefiev, V., et al. 2021, *A&A*, 647, A1, doi: [10.1051/0004-6361/202039313](https://doi.org/10.1051/0004-6361/202039313)
- Prigozhin, G., Gendreau, K., Doty, J. P., et al. 2016, in *Society of Photo-Optical Instrumentation Engineers (SPIE) Conference Series*, Vol. 9905, *Space Telescopes and Instrumentation 2016: Ultraviolet to Gamma Ray*, ed. J.-W. A. den Herder, T. Takahashi, & M. Bautz, 99051I, doi: [10.1117/12.2231718](https://doi.org/10.1117/12.2231718)
- Ransom, S. 2011, *PRESTO: Pulsar Exploration and Search Toolkit*. <http://ascl.net/1107.017>
- Ransom, S. M., Eikenberry, S. S., & Middleditch, J. 2002, *AJ*, 124, 1788, doi: [10.1086/342285](https://doi.org/10.1086/342285)
- Rao, A., Paice, J. A., Gandhi, P., & Beri, A. 2019, *The Astronomer's Telegram*, 12821, 1

- Ratti, E. M., Jonker, P. G., Miller-Jones, J. C. A., et al. 2012, *MNRAS*, 423, 2656, doi: [10.1111/j.1365-2966.2012.21071.x](https://doi.org/10.1111/j.1365-2966.2012.21071.x)
- Remillard, R. A., & McClintock, J. E. 2006, *ARA&A*, 44, 49, doi: [10.1146/annurev.astro.44.051905.092532](https://doi.org/10.1146/annurev.astro.44.051905.092532)
- Remillard, R. A., Loewenstein, M., Steiner, J. F., et al. 2021, arXiv e-prints, arXiv:2105.09901. <https://arxiv.org/abs/2105.09901>
- Russell, D. M., Russell, T. D., Miller-Jones, J. C. A., et al. 2013, *ApJL*, 768, L35, doi: [10.1088/2041-8205/768/2/L35](https://doi.org/10.1088/2041-8205/768/2/L35)
- Russell, T. D., Soria, R., Motch, C., et al. 2014, *MNRAS*, 439, 1381, doi: [10.1093/mnras/stt2480](https://doi.org/10.1093/mnras/stt2480)
- Sato, R., Serino, M., Nakahira, S., et al. 2012, *The Astronomer's Telegram*, 4024, 1
- Shaw, A. W., Tetarenko, B. E., Dubus, G., et al. 2019, *MNRAS*, 482, 1840, doi: [10.1093/mnras/sty2787](https://doi.org/10.1093/mnras/sty2787)
- Shidatsu, M., Ueda, Y., Nakahira, S., et al. 2013, *ApJ*, 779, 26, doi: [10.1088/0004-637X/779/1/26](https://doi.org/10.1088/0004-637X/779/1/26)
- Sidoli, L., Paizis, A., Mereghetti, S., Götz, D., & Del Santo, M. 2011, *MNRAS*, 415, 2373, doi: [10.1111/j.1365-2966.2011.18865.x](https://doi.org/10.1111/j.1365-2966.2011.18865.x)
- Soleri, P., Muñoz-Darias, T., Motta, S., et al. 2013, *MNRAS*, 429, 1244, doi: [10.1093/mnras/sts405](https://doi.org/10.1093/mnras/sts405)
- Steiner, J. F., García, J. A., Eikmann, W., et al. 2017, *ApJ*, 836, 119, doi: [10.3847/1538-4357/836/1/119](https://doi.org/10.3847/1538-4357/836/1/119)
- Steiner, J. F., Narayan, R., McClintock, J. E., & Ebisawa, K. 2009, *PASP*, 121, 1279, doi: [10.1086/648535](https://doi.org/10.1086/648535)
- Sugizaki, M., Mihara, T., Serino, M., et al. 2011, *PASJ*, 63, S635, doi: [10.1093/pasj/63.sp3.S635](https://doi.org/10.1093/pasj/63.sp3.S635)
- Sunyaev, R., & Revnivtsev, M. 2000, *A&A*, 358, 617. <https://arxiv.org/abs/astro-ph/0003308>
- Sunyaev, R., Arefiev, V., Babushkin, V., et al. 2021, arXiv e-prints, arXiv:2104.13267. <https://arxiv.org/abs/2104.13267>
- Swank, J. H. 1999, *Nuclear Physics B Proceedings Supplements*, 69, 12, doi: [10.1016/S0920-5632\(98\)00175-3](https://doi.org/10.1016/S0920-5632(98)00175-3)
- Tanaka, Y., & Shibazaki, N. 1996, *ARA&A*, 34, 607, doi: [10.1146/annurev.astro.34.1.607](https://doi.org/10.1146/annurev.astro.34.1.607)
- Tetarenko, B. E., Dubus, G., Lasota, J. P., Heinke, C. O., & Sivakoff, G. R. 2018a, *MNRAS*, 480, 2, doi: [10.1093/mnras/sty1798](https://doi.org/10.1093/mnras/sty1798)
- Tetarenko, B. E., Dubus, G., Marcel, G., Done, C., & Clavel, M. 2020, *MNRAS*, 495, 3666, doi: [10.1093/mnras/staa1367](https://doi.org/10.1093/mnras/staa1367)
- Tetarenko, B. E., Lasota, J. P., Heinke, C. O., Dubus, G., & Sivakoff, G. R. 2018b, *Nature*, 554, 69, doi: [10.1038/nature25159](https://doi.org/10.1038/nature25159)
- Tetarenko, B. E., Sivakoff, G. R., Heinke, C. O., & Gladstone, J. C. 2016, *ApJS*, 222, 15, doi: [10.3847/0067-0049/222/2/15](https://doi.org/10.3847/0067-0049/222/2/15)
- Tonry, J., Denneau, L., Heinze, A., et al. 2019, *Transient Name Server Discovery Report*, 2019-2553, 1
- van der Klis, M. 1988, in *Timing Neutron Stars*, Vol. 262, 27–70
- van der Klis, M. 2006, *Rapid X-ray Variability*, Vol. 39, 39–112
- van Doesburgh, M., van der Klis, M., & Morsink, S. M. 2018, *MNRAS*, 479, 426, doi: [10.1093/mnras/sty1404](https://doi.org/10.1093/mnras/sty1404)
- van Paradijs, J. 1996, *ApJL*, 464, L139, doi: [10.1086/310100](https://doi.org/10.1086/310100)
- van Velzen, S., Bellm, E. C., & van Roestel, J. 2019, *The Astronomer's Telegram*, 12796, 1
- Wang-Ji, J., García, J. A., Steiner, J. F., et al. 2018, *ApJ*, 855, 61, doi: [10.3847/1538-4357/aaa974](https://doi.org/10.3847/1538-4357/aaa974)
- Wijnands, R., Degenaar, N., Armas Padilla, M., et al. 2015, *MNRAS*, 454, 1371, doi: [10.1093/mnras/stv1974](https://doi.org/10.1093/mnras/stv1974)
- Wilkes, B., & Tucker, W., eds. 2019, *The Chandra X-ray Observatory*, 2514-3433 (IOP Publishing), doi: [10.1088/2514-3433/ab43dc](https://doi.org/10.1088/2514-3433/ab43dc)
- Wilms, J., Allen, A., & McCray, R. 2000, *ApJ*, 542, 914, doi: [10.1086/317016](https://doi.org/10.1086/317016)
- Winkler, C., Courvoisier, T. J. L., Di Cocco, G., et al. 2003, *A&A*, 411, L1, doi: [10.1051/0004-6361:20031288](https://doi.org/10.1051/0004-6361:20031288)
- Yadlapalli, N., Ravi, V., Yao, Y., Kulkarni, S. R., & Brisken, W. 2021, *ApJL*, 909, L27, doi: [10.3847/2041-8213/abea19](https://doi.org/10.3847/2041-8213/abea19)
- Yao, Y., Garcia, J., Grefenstette, B., et al. 2020a, *The Astronomer's Telegram*, 13957, 1
- Yao, Y., Enoto, T., Altamirano, D., et al. 2020b, *The Astronomer's Telegram*, 13932, 1
- Yao, Y., Kulkarni, S. R., Burdge, K. B., et al. 2020c, arXiv e-prints, arXiv:2012.00169. <https://arxiv.org/abs/2012.00169>
- Yao, Y., De, K., Kasliwal, M. M., et al. 2020d, *ApJ*, 900, 46, doi: [10.3847/1538-4357/abaa3d](https://doi.org/10.3847/1538-4357/abaa3d)
- Zhang, L., Altamirano, D., Cúneo, V. A., et al. 2020a, *MNRAS*, 499, 851, doi: [10.1093/mnras/staa2842](https://doi.org/10.1093/mnras/staa2842)
- Zhang, S.-N. 2013, *Frontiers of Physics*, 8, 630, doi: [10.1007/s11467-013-0306-z](https://doi.org/10.1007/s11467-013-0306-z)
- Zhang, S.-N., Li, T., Lu, F., et al. 2020b, *Science China Physics, Mechanics, and Astronomy*, 63, 249502, doi: [10.1007/s11433-019-1432-6](https://doi.org/10.1007/s11433-019-1432-6)